# Accelerating Diffusion-Weighted Chemical Shift Imaging using Compressed Sensing with Parameter Mapping

Master's Thesis

J.W.F. van der Kemp

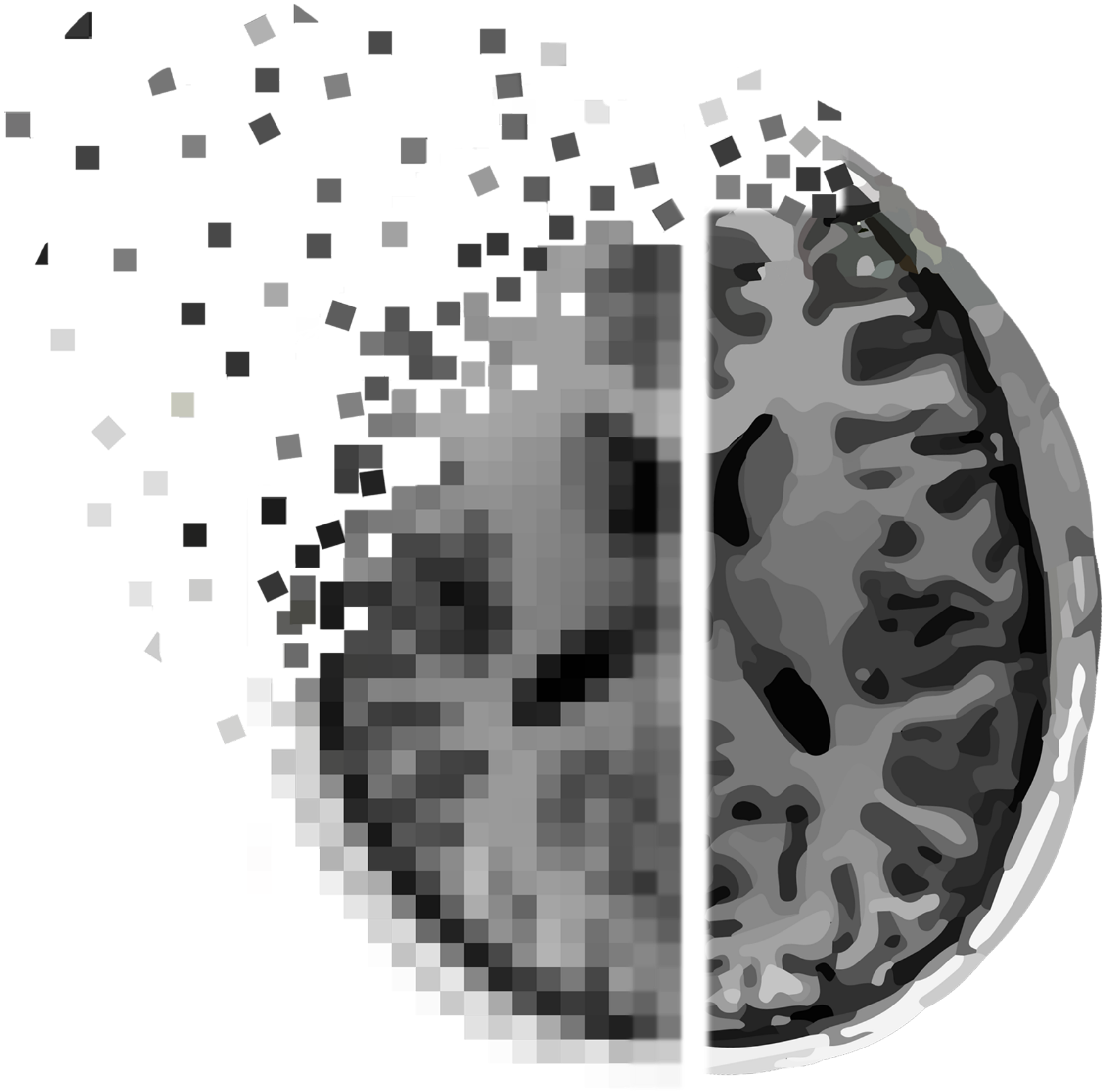

# Accelerating Diffusion-Weighted Chemical Shift Imaging using Compressed Sensing with Parameter Mapping

## Master's Thesis

by

**J.W.F. van der Kemp**

at the Circuits and Systems group
of the faculty Electrical Engineering, Mathematics and Computer Science
from Delft University of Technology,
in collaboration with the C.J.Gorter Center for High-field MRI
of Leiden University Medical Center.

In partial fulfillment of the requirements for the degree of

**Master of Science**
in Electrical Engineering - *Signals & Systems*

at the Delft University of Technology,
to be defended publicly on Thursday October 13th, 2016 at 10:00 AM.

| | | |
|---|---|---|
| Student number: | 4104455 | |
| Project duration: | January 2016 – October 2016 | |
| Thesis committee: | Prof. dr. P. Börnert, | Philips Research Hamburg |
| | Dr. ir. R. Remis, | TU Delft, *supervisor* |
| | Dr. I. Ronen, | LUMC, *supervisor* |
| | Prof. dr. ir. A.J. van der Veen, | TU Delft |

# Abstract

Diffusion-weighted chemical shift imaging (DW-CSI) is a recently developed MRI modality that enables radiologists to reveal the diffusion properties of small molecules that act in metabolic reactions in-vivo. In order to extract this diffusion information from a patient, DW-CSI requires approximately one hour of scan time. This extensive scan time makes DW-CSI currently inapplicable for the clinical setting. This thesis describes the closely intertwined implementation of compressed sensing with parameter mapping (CS-PM) in the DW-CSI processing pipeline to accelerate its acquisition. The CS-PM algorithm enables DW-CSI to acquire less measurements (sample under Nyquist) and subsequently reconstruct the missing samples with the use of a custom designed, model-based sparsifying dictionary. As proof of concept, CS-PM was evaluated on the water signal of a non-water-suppressed DW-CSI scan. The results of the integration of CS-PM in the DW-CSI processing pipeline already indicates a feasible acceleration factor of 1.5 (scan time reduction of ca. 20 minutes) along with valuable insight to further improve the performance of DW-CSI in combination with CS-PM.

# Preface

In the thesis you have in front of you, I will explain the research I have performed for my final project for the Master's degree in Electrical Engineering with a specialisation in the signal processing of medical images. This research project was conducted at the Circuits and Systems group of the Delft University of Technology (TU Delft) in collaboration with the C.J.Gorter Center for High-field MRI of the Leiden University Medical Center (LUMC). The C.J.Gorter Center is an academic research group that aims to develop new techniques for high-field clinical applications of MRI with a Philips Achieva 7 tesla whole body MRI scanner as their playground.

The aim of the research project was to speedup the scan time of a new MRI modality. This new MRI modality is diffusion-weighted chemical shift imaging, short DW-CSI, and is developed by inter alia my LUMC supervisor Itamar Ronen. DW-CSI can give insight about the diffusion properties of small particles in the human brain, however its scan time is currently a major bottleneck to adopt DW-CSI in a clinical setting. To indirectly speedup the scan time, I have implemented a reconstruction algorithm to estimate the diffusion properties from a reduced measurement set. This, because in MRI the number of measurements is proportional to the scan time.

During this project I have learned a great deal about scientific research, adequate problem solving, working in the academic environment and of course magnetic resonance imaging. Frustratingly enough, I have not been able to meet the acceleration as I initially hoped for. On the other hand, Itamar and I have gained considerable insight in the possibilities to further accelerate DW-CSI. This research topic is to be continued.

This work was evaluated by the thesis committee composed of Prof. dr. Peter Börnert from Philips Research Hamburg and Gorter Center visiting Professor, Dr. ir. Rob Remis from Circuits and Systems TU Delft, Dr. Itamar Ronen from the Gorter Center and Prof. dr. ir. Alle-Jan van der Veen head of Circuits and Systems TU Delft.

Looking back at the labor and time associated with this thesis, I would like to acknowledge Rob Remis and Itamar Ronen for their supervision, input and reflexion. I further would like to thank the Gorter group for keeping up the spirit up during these nine months of solitude with the after-work drinks; Reijer Leijsen for the access to the coffee machine at the TU Delft that kept us going during our projects; Margina Ruiter for designing the artwork of this thesis and the friends I have tortured in the MR scanner to extract their diffusion brain data.

At last, I would like to thank you, the reader, since you took the courage to open my thesis and already have read at least one page. Thank you.

*Joost van der Kemp*
*Delft, October 2016*

# Contents

**List of Figures** ix

**List of Abbreviations** xi

**1 Introduction** 1
1.1 Problem Statement 2
1.2 Project Goal 2
1.3 Thesis Outline 2

**2 Background of DW-CSI** 3
2.1 Magnetic Resonance Imaging 3
2.1.1 Chemical Shift Imaging 4
2.2 Diffusion-Weighted Chemical Shift Imaging 5
2.2.1 Pulse Sequence 5
2.2.2 Post-processing 7
2.2.3 Data Analysis 9

**3 Scan Time Reduction Algorithms** 11
3.1 Parallel Imaging 11
3.2 Compressed Sensing 11
3.3 Parallel Imaging meets Compressed Sensing 12
3.4 Compressed Sensing Parameter Mapping 12

**4 Compressed Sensing Parameter Mapping for DW-CSI** 13
4.1 Acquisition and Initial Post-Processing 13
4.1.1 Phase Encoding Undersampling Pattern 14
4.1.2 Roemer Reconstruction 14
4.2 Reconstruction 16
4.2.1 Compressed Sensing in MRI 16
4.2.2 *k*-*p* space 17
4.2.3 Sparsity 17
4.2.4 Dictionary 18
4.2.5 Orthogonal Matching Pursuit 19
4.2.6 Regularization 19
4.2.7 Reconstruction Algorithm 20

**5 Results & Evaluation** 21
5.1 Data 21
5.1.1 Synthetic Data 21
5.1.2 Acquired Data 22
5.2 Results 23
5.2.1 Dictionary 23
5.2.2 Parameter Mapping 24
5.2.3 Roemer Reconstruction 25
5.2.4 Phase Encoding Undersampling Pattern 25
5.2.5 Compressed Sensing Parameter Mapping 26
5.2.6 Regularization 27

6 Discussion & Conclusion 31

Bibliography 33

A Aliasing Artifact Distributions after *SNR*-Phase Combination 37

B Aliasing Artifact Distributions after Roemer Reconstruction 41

# List of Figures

1.1 DW-CSI acquisition & processing . . . 1

2.1 MR scanner . . . 3
2.2 MRI: $k$-space & image space . . . 4
2.3 MR spectroscopy . . . 4
2.4 VAPOR scheme . . . 5
2.5 PRESS volume selection . . . 6
2.6 PRESS-based DW-CSI pulse sequence . . . 7
2.7 Metabolite $ADC$-maps . . . 9

4.1 Phase encoding undersampling patterns . . . 14
4.2 Construction of coil sensitivity maps . . . 15
4.3 Compressed sensing reconstruction . . . 17
4.4 Cartesian full and undersampled $k$-$p$ space . . . 18
4.5 Dictionary $\mathbf{\Psi}$ . . . 19

5.1 Synthetic DW-CSI data . . . 21
5.2 Plan DW-CSI scan . . . 22
5.3 Acquired DW-CSI data . . . 22
5.4 Dictionary validation . . . 23
5.5 Parameter mapping validation . . . 24
5.6 Direct parameter mapping on full $H_2O$ scan . . . 24
5.7 CSI images with Roemer reconstruction . . . 24
5.8 $ADC$-map with Roemer reconstruction . . . 25
5.9 PE undersampling error of DW-CSI images . . . 26
5.10 PE undersampling error of DW-CSI images with Roemer reconstruction . . . 26
5.11 DW-CSI image of CS-PM reconstruction without regularization . . . 27
5.12 CS-PM on full $H_2O$ scan . . . 28
5.13 CS-PM on full $H_2O$ scan with Roemer reconstruction . . . 29

A.1 Histograms PE undersampled vs full difference *before* post-processing . . . 38
A.2 Histograms PE undersampled vs full difference *after* post-processing . . . 39

B.1 Histograms PE undersampled vs full difference *before* post-processing (Roemer recon.) 42
B.2 Histograms PE undersampled vs full difference *after* post-processing (Roemer recon.) 43

# List of Abbreviations

**2D** two-dimensional

**3D** three-dimensional

*ADC* apparent diffusion coefficient

**a.u.** arbitrary units

**BART** Berkeley Advanced Reconstruction Toolbox

**BLUE** best linear unbiased estimator

**CHESS** chemical shift-selective

**Cho** choline

**Cr** creatine

**CRLB** Cramér-Rao lower bound

**CS** compressed sensing

**CSI** chemical shift imaging

**CSM** coil sensitivity map

**CS-PM** compressed sensing parameter mapping

**DW-CSI** diffusion-weighted chemical shift imaging

**ESPIRiT** efficient L1-SPIRiT

**FID** free induction decay

**FOV** field-of-view

**GRAPPA** generalized autocalibrating partial parallel acquisition

**$H_2O$** dihydrogen monoxide (water)

**ISMRM** International Society for Magnetic Resonance in Medicine

**LCModel** linear combination of the model (in vitro spectra)

**LPSVD** linear prediction singular value decomposition

**LUMC** Leiden University Medical Center

**MATLAB** Matrix Laboratory (The MathWorks, Inc.)

**MIP** maximum intensity projection

**MR** magnetic resonance

**MRI** magnetic resonance imaging

**NAA** N-acetylaspartate

**NRMSE** normalized root mean square error

**OMP** orthogonal matching pursuit

**PDF** probability density function

**PE** phase encoding

**PI** parallel imaging

**PM** parameter mapping

**ppm** parts per million

**PPU** peripheral pulse unit

**PRESS** point-resolved spectroscopy

**RF** radio frequency

**SENSE** sensitivity encoding

$SNR$ signal-to-noise ratio

**SPIRiT** iterative self-consistent parallel imaging reconstruction

**TE** echo time

**TR** repetition time

**VAPOR** variable power and optimized relaxation delays

**VOI** volume-of-interest

**voxel** volume element

# 1

# Introduction

Magnetic resonance imaging (MRI) is a medical imaging modality with countless measurement configurations and possibilities. One of these MR measurements is the recently developed diffusion-weighted chemical shift imaging (DW-CSI) at a magnetic field strength of 7T. DW-CSI is a unique tool for the noninvasive exploration of the structure and physiology of the intracellular space in vivo [1–4]. This clinically valuable insight is achieved since DW-CSI is able to measure and quantify the diffusion properties of intracellular metabolites, such as N-acetylaspartate (NAA), choline (Cho) and creatine (Cr). An informative diffusion property is the apparent diffusion coefficient (*ADC*). A brief schematic description of DW-CSI is provided in Figure 1.1, the elements in this figure will be explained in more detail in the following chapters.

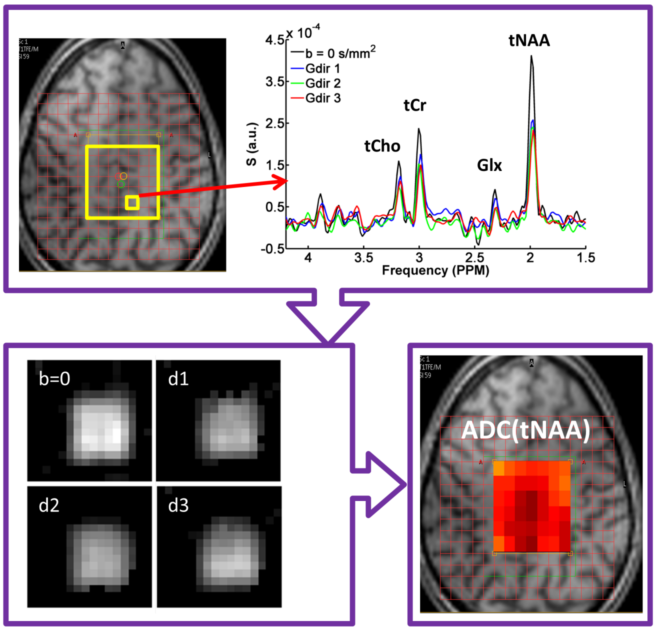

Figure 1.1: Schematic description of the acquisition and processing overview for DW-CSI [1].
The first block visualizes the anatomical planning of a DW-CSI scan with in yellow the volume-of-interest (VOI) within the larger red grid of the field-of-view (FOV). Of one voxel the acquired chemical shift spectra are depicted under their different diffusion conditions. The second block shows the CSI images of the total NAA under the different diffusion conditions derived from the spectra. The last block shows the resulting *ADC*-map derived from the diffusion-weighted CSI images.

## 1.1. Problem Statement

In order to estimate the *ADC* of certain metabolites, multiple spectroscopy scans are required under various diffusion conditions. In addition, since MR acquisitions are already time restricted due to the intrinsic properties of the tissue being examined (as $T_1$ time), the extensive scan time (ca. 1 hour) becomes a cumbersome issue for DW-CSI. The long scan time counteracts with the patient's comfort as well as the signal-to-noise ratio (*SNR*) of the *ADC*-map due to inter alia patient movement. Thus, in order to make DW-CSI more applicable for the clinical setting, the scan time will have to be reduced.

Because the scan time in MR is proportional to the number of separate acquisitions with their phase encodings (PEs), a straightforward manner to reduce the scan time is to reduce the number of PEs. Parallel imaging (PI) and compressed sensing (CS) showed to be successful reconstruction approaches to work with a reduced number of PE without reducing the spectral resolution [5, 6].

## 1.2. Project Goal

The goal of this thesis project is to implement a signal reconstruction algorithm to accelerate the DW-CSI acquisition and estimate the *ADC*-map. We will combine prior DW-CSI knowledge and the algorithms of PI and CS achieve this goal.

## 1.3. Thesis Outline

In **Chapter 2: Background of DW-CSI** we will first set forth the background knowledge for this thesis beginning with a brief introduction to MRI and CSI followed by a more in depth explanation of DW-CSI: from acquisition to *ADC*-map.

In **Chapter 3: Scan Time Reduction Algorithms** possible algorithms will be discussed with their applicability to DW-CSI to reduce the scan time.

In **Chapter 4: Compressed Sensing Parameter Mapping for DW-CSI** we will present our proposed acceleration method: compressed sensing parameter mapping together with its adjustments to the conventional DW-CSI.

In **Chapter 5: Results & Evaluation** the compressed sensing parameter mapping algorithm with all its subelements will be evaluated according to synthetic and acquired in-vivo data.

In **Chapter 6: Discussion & Conclusion** we will further discuss and conclude the performance of the compressed sensing parameter mapping method to accelerate the DW-CSI acquisition.

# 2

# Background of DW-CSI

In this chapter we briefly set forth the concepts of magnetic resonance imaging required for this thesis, followed by its extension to chemical shift imaging. Subsequently, diffusion-weighted chemical shift imaging as described in the paper by Ercan et al. (2014) [1] will be explained. The DW-CSI acquisition pulse sequence will be set forth followed by the post-processing with eventually the data analysis with the calculation of the apparent diffusion coefficient.

## 2.1. Magnetic Resonance Imaging

Magnetic resonance imaging (MRI) is a noninvasive medical imaging technique which exploits the magnetic properties of the human body [8, 9]. As visual reference a cutaway of an MR scanner is displayed in Figure 2.1. An MR scanner uses a strong, static magnetic field ($B_0$) to align the magnetic moments of protons in the body in the direction of this magnetic field. When a radio frequency (RF) pulse is applied where its frequency matches the precession frequency of the protons in the body, the magnetic moments of the protons change. This precession frequency (or Larmor frequency $f_0$) of the protons is defined as

$$f_0 = \gamma B_0 \tag{2.1}$$

where $\gamma$ is the gyromagnetic ratio of the nucleus and $B_0$ the external magnetic field. Since water is abundant in the human body, the gyromagnetic ratio of hydrogen ($\gamma_{\{^1\mathrm{H}\}} = 42.58$ MHz/T) is selected for most MRI scans. After the RF pulse is applied, the magnetic moments of the protons will recover to their equilibrium according to the external magnetic field, emitting a RF pulse: the free induction decay (FID). This FID is the signal that is measured in MRI and its magnitude depends on the amount of protons in the body. However, in this manner it is yet only possible to measure the "bulk" signal and it is not possible to distinguish where in the body the signals originate from. In order to resolve

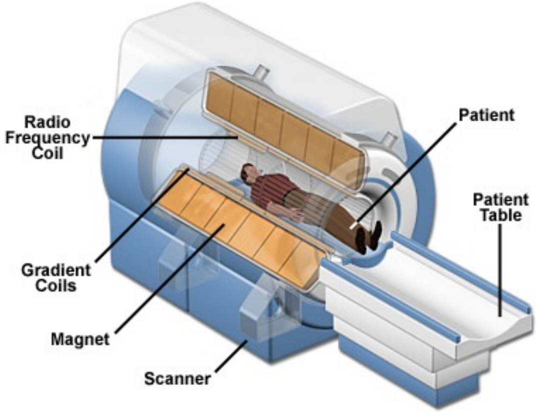

Figure 2.1: MR scanner and its principal components [7].

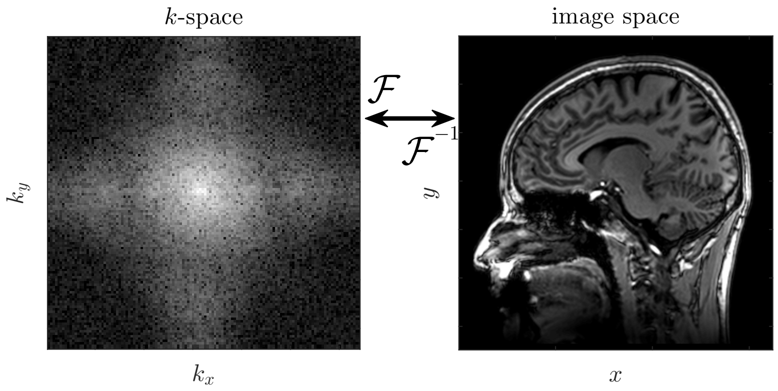

Figure 2.2: $k$-space and image space with their Fourier transform ( $\mathcal{F}$ ) relation.

this, the gradient coils in the scanner slightly alter the static $B_0$ field spatially, inducing a change in the Larmor frequency. These gradient fields generated by the gradient coils can be applied during the RF pulse, creating spatial selective excitation, as well as after the RF pulse while the magnetic moments of the protons are recovering to induce phase and frequency encoding in the measured signal (readout). With these steps, the MR scanner is able to measure the frequency components of the desired image or volume. In other words: the scanner is able to measure the Fourier space of the desired image, or in MRI jargon: $k$-space. The relation between the desired image and the raw measured $k$-space is visualized in Figure 2.2.

### 2.1.1. Chemical Shift Imaging

The technique for imaging can be extended to magnetic resonance (MR) spectroscopic imaging, also called chemical shift imaging (CSI). With CSI different nuclei can be distinguished by their chemical frequency shift [10]. The chemical shift is expressed in parts per million (ppm) with respect to the Larmor frequency. This unit of measurement has the advantage that the expressed chemical shift is independent of the MR system with its magnetic field. In a CSI acquisition, the MR scanner spatial selectively excites the volume-of-interest (VOI) and phase encodes a single location in $k$-space. The subsequent acquired signals contain the phase encoded free induction decays (FIDs) of the nuclei in the excited VOI and span $k$-space. After a spatial inverse- and a temporal forward Fourier transform, the spectroscopy dataset emerges. This dataset contains a spectroscopy readout at each voxel in the VOI. However, in order to reveal the signals originating from small metabolites of interest, which are currently overshadowed by the abundant water signal, a water suppression pulse sequence will have to be applied prior to each acquisition. An example of a resulting dataset with water suppression is visualized in Figure 2.3. If, for example, the signal peak around the NAA resonance (2.0 ppm) is integrated, an image can be formed indicating the relative quantities of total NAA in those voxels. The next section will explain CSI in more detail within the framework of DW-CSI.

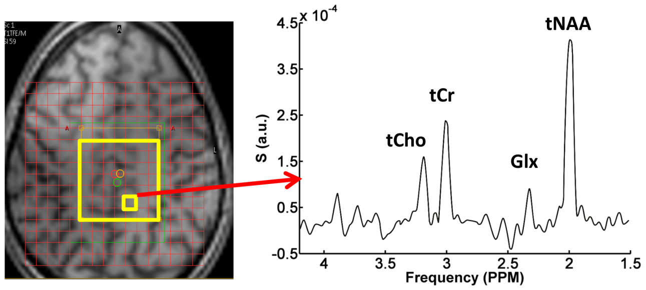

Figure 2.3: MR spectroscopy example based on Figure 1.1.
The left part visualizes the anatomical planning of a CSI scan with in yellow the volume-of-interest (VOI) within the larger red grid of the field-of-view (FOV). The right part depicts the acquired CSI spectra of one voxel.

## 2.2. Diffusion-Weighted Chemical Shift Imaging

As briefly explained in the Introduction, diffusion-weighted chemical shift imaging can reveal location specific diffusion properties of small molecules that act in metabolic reactions, the metabolites. This section will set forth how DW-CSI is able to measure and analyze this. First the MR pulse sequence is explained that makes it able to measure the signals that contain the diffusion properties of the metabolites. Subsequently, these acquired signals are corrected for artifacts from the acquisition in the post-processing. Finally, the $ADC$-map is calculated from the corrected signals in the data analysis.

### 2.2.1. Pulse Sequence

In order to extract the diffusion properties from a subject in the scanner, an MR pulse sequence is developed consisting of several blocks. The following paragraphs will set forth and explain these elements.

**VAPOR** First, the variable power and optimized relaxation delays (VAPOR) [11] water suppression sequence is applied. The VAPOR sequence consists of seven consecutive chemical shift-selective (CHESS) RF pulses with varying power. CHESS uses a frequency-selective 90° RF pulse to selectively excite the water signal followed by a spoiler gradient, which causes the transverse water magnetization to dephase, as illustrated in Figure 2.4. This makes it possible to acquire the signal from the metabolites, which otherwise would have been overshadowed by the water signal.

In the DW-CSI scheme, the VAPOR sequence is slightly deoptimized to retain a small amount of the water signal in the FID. The deoptimization is achieved by increasing the delay between the last VAPOR pulse and the excitation pulse to 250 ms. The information in the water signal allows us to correct for eddy currents in the acquisition later in the post-processing.

**PRESS** After the VAPOR pulse train, the DW-CSI scan is mainly based on the point-resolved spectroscopy (PRESS) [12] sequence. PRESS excites the preselected volume-of-interest (VOI) by applying slab selection in three spatial dimensions: a 90° RF pulse with two subsequent 180° pulses each under a gradient field perpendicular to the previous. In this way, only the volume under the three overlapping perpendicular slices is exited as demonstrated in Figure 2.5. After exiting the VOI, phase encoding is applied within the larger field-of-view (FOV) to later distinguish the spatial origin of the signals.

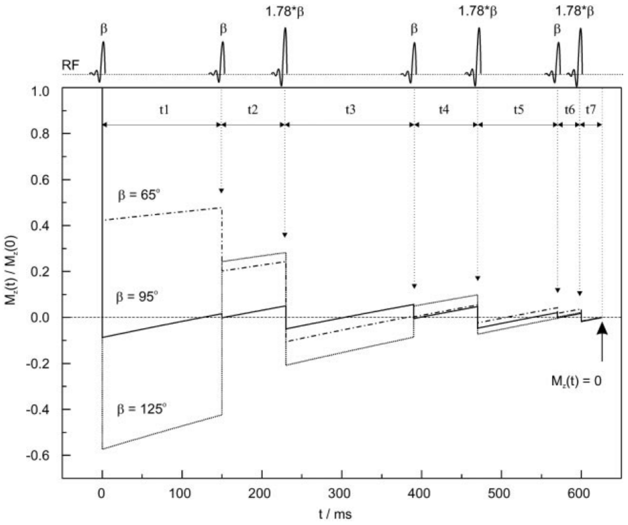

Figure 2.4: VAPOR sequence illustrated with its effect on the water $M_Z$ magnetization after applying each of the seven CHESS varying power RF pulses to suppress this water signal [11]. Three different values of nominal flip angles ($\beta$ = {65°, 95°, 125°}) are depicted as example.

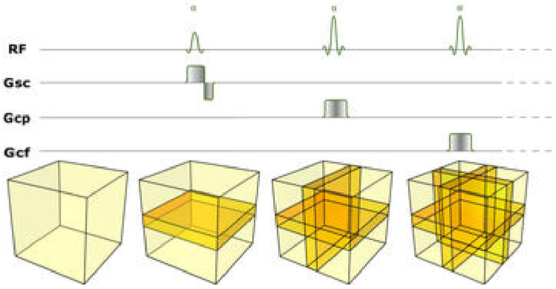

Figure 2.5: Principles of volume selection visualized [13].

**DW-PRESS** The extension from regular spectroscopy to spectroscopy under different diffusion conditions is achieved by applying bipolar diffusion gradients around the two PRESS 180° RF pulses. The pair of opposite operating diffusion gradients around the first 180° pulse induce a location specific phase offset in the transverse magnetization. The pair of diffusion gradients around the second 180° pulse tries to refocus this. After these two de- and refocusing diffusion gradient pairs, the net phase shift of stationary molecules is zero. However, any molecules which spatially drifted (diffused) will have a phase offset. This phase offset is dependent on the net travelled distance of the molecules within a voxel (the diffusion coefficient $D$), the time between the two 180° pulses ($\Delta$), the ON-time of one diffusion gradient pair ($\delta$), the time delay between the opposite gradients of one pair ($\tau$) and the gradient amplitude ($g$) of the applied diffusion gradients. The last four parameters can be controlled and expressed in the $b$-value which depicts the diffusion condition of a scan [14]. This $b$-value is determined by

$$b = \gamma^2 g^2 \delta^2 \left( \Delta - \frac{\delta}{3} - \frac{\tau}{2} \right) \tag{2.2}$$

and is expressed in time/area [s/mm$^2$]. In this equation, $\gamma$ represents the gyromagnetic ratio of the observed nucleus. After the applied diffusion gradients, the resulting acquired signal can be modeled as an exponential decayed version of the signal at baseline, formulated as

$$S(b) = S_0 \, e^{-bD} \tag{2.3}$$

where the signal at baseline is defined as $S_0 = S(b = 0)$. However, the estimation of $D$ is very susceptible to noise, considering the already small signals from the metabolites. Furthermore, the parameters $D$ and $b$ are directional dependent, given the cellular physiology and microanatomy. Therefore, in this implementation, the apparent diffusion coefficient ($ADC$) is used to describe the average diffusion rate and is estimated from the measurements as

$$ADC = -\frac{1}{n} \sum_{i=1}^{n} \frac{\ln\left(\frac{S(b_i)}{S_0}\right)}{b_i} \tag{2.4}$$

with the different $b$-values applied with equal magnitude in $n$ directions and the $ADC$-value expressed in area/time [mm$^2$/s]. These $ADC$-values will be estimated later on in the data analysis from the post-processed measurements and visualized in an $ADC$-map.

**Navigator** To improve the stability of the DW-CSI measurements, navigators were introduced to the scheme [1]. These navigators are small samples (ca. 25-30 data points) taken after the applied VAPOR and DW-PRESS sequence and prior to the PE and its consecutive readout. Depending on the navigator, the subsequent readout is accepted or rejected in real time. This navigator-based accept/reject strategy is valuable because it can detect corrupted signals due to bulk motion (e.g. patient movement and the pulsating of the brain [15]). During the applied diffusion gradients, linear motion will result in a phase fluctuation on the readout and rotational movement will result in an amplitude fluctuation in the readout [3]. The amplitude fluctuations are very hard to correct for and a reacquisition is required. The phase fluctuations can be corrected in the post-processing using the information from the navigators. For each diffusion condition, the sum of the moduli of six navigator data points (points 5-10) is calculated. The highest sum of the first five acquisitions is selected as amplitude

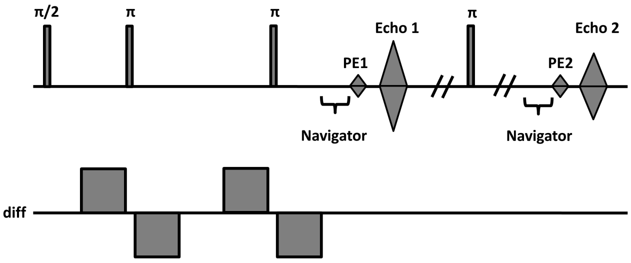

Figure 2.6: Schematic representation of the two echo acquisition DW-CSI pulse sequence with bipolar diffusion gradients around the two 180° PRESS RF pulses [1]. The navigators are acquired prior to the phase encoding steps. Note that the VAPOR sequence is located prior to the first 90° PRESS RF pulse.

reference. For the accept/reject criterion, the navigator threshold is empirically defined as 85% of this amplitude reference. An upper bound of 100 reacquisitions is set for each diffusion condition to restrict the scan time.

**Cardiac Triggering** In order to reduce the influence of the pulsating of the brain, and thereby the possible navigator-based rejections, the DW-CSI scheme is cardiac triggered. The cardiac cycle is measured by a peripheral pulse unit (PPU) on the finger of the subject. The first MR excitation pulse of each acquisition is applied 230 ms after each trigger to minimize the amplitude fluctuations [3].

**DW-CSI Sequence** This brings us to the pulse and diffusion gradient sequence as depicted in Figure 2.6. Note that this is a spectroscopy imaging mode with two phase encoded echo acquisitions. Eventually, for each DW-CSI measurement, five consecutive scans are acquired with different settings in this sequence:

- one CSI scan without water suppression,
  without an applied diffusion condition ($b = 0$ s/mm$^2$);
- one CSI scan with water suppression,
  without an applied diffusion condition ($b = 0$ s/mm$^2$);
- three CSI scan with water suppression,
  with different diffusion conditions in observed diffusion directions.

In these non-PE reduced (conventional) scans, $k$-space (12 × 12) is filled with a spiral PE trajectory to include circular $k$-space coverage. In practice the total scan time of these acquisitions is about one hour, though varies as a result of of the real-time navigator-based reacquisitions and the cardiac triggering.

### 2.2.2. Post-processing

With the subject scanned, the acquired DW-CSI data is exported as raw data (*.DATA*/*.LIST* in Philips format). In this raw data, each readout contains the navigator, $Nav^{\{0\}}_{ij,m,c}(t)$, and the subsequent FID, $s^{\{0\}}_{ij,m,c}(t)$, in one array of each location in $k$-space, $(i, j)$, from each individual receive coil $c$, for each scan with diffusion condition $m$, formulated as

$$READOUT^{\{0\}}_{ij,m,c}(t) = \left[Nav^{\{0\}}_{ij,m,c}(t),\ s^{\{0\}}_{ij,m,c}(t)\right] \tag{2.5}$$

where the superscript {0} indicates the raw unprocessed data.

To perform the offline analysis the raw data is imported into MATLAB. Here, all the readouts span the $k$-space-time domain matrices for each scan. The next seven paragraphs, will explain the MATLAB post-processing steps. Several blocks will preform corrections on the data, altering the FID ($s_{ij,m}(t)$) or spectrum ($S_{xy,m}(f)$) in $k$-space ($s_{ij}$) or image space ($s_{xy}$) of a scan with diffusion condition $m$. The result of each process on $s(t)$ will be marked with the superscript of that block. Thus, the phase fluctuation corrected FID of paragraph (c) will be depicted as: $s^{\{c\}}_{ij,m}(t)$.

(a) **Combine parallel data.** First, the data of the 32 separate receive coils is combined to one dataset. This procedure is performed as

$$READOUT^{\{a\}}_{ij,m}(t) = \sum_{c=1}^{32} \frac{|\, READOUT^{\{0\}}_{(0,0),m,c}(0) \,|}{\sum_{c'=1}^{32} |\, READOUT^{\{0\}}_{(0,0),m,c'}(0) \,|} \cdot \frac{READOUT^{\{0\}}_{ij,m,c}(t)}{e^{\mathrm{i}\angle READOUT^{\{0\}}_{(0,0),m,c}(0)}} \tag{2.6}$$

and combines the readouts at each PE according to the $SNR$ and phase of each receive coil.

(b) **Navigator processing.** Next, the navigators under each PE and each diffusion condition are extracted from the dataset, zero padded to 128 points and line-broadened in the temporal direction, as

$$Nav^{\{b\}}_{ij,m}(t) = Nav^{\{a\}}_{ij,m}(t) \cdot e^{-\pi\, l_b\, t} \tag{2.7}$$

where $Nav^{\{b\}}_{ij,m}(t)$ is the zero padded, line-broadened navigator and $l_b \approx 50$ Hz. After a temporal Fourier transform, the phase of the navigator ($\theta_{Nav}(ij, m)$) is estimated from the complex integral around the residual water peak (ca. 7 points).

(c) **Correct phase fluctuations.** With the phase of the navigators known at each location in $k$-space at each diffusion condition, the diffusion-induced phase fluctuations can be corrected. This is accomplished by multiplying the FID ($s^{\{a\}}_{ij,m}$) with the navigator-based phase correction factor given by

$$s^{\{c\}}_{ij,m}(t) = s^{\{a\}}_{ij,m}(t) \cdot \frac{e^{\mathrm{i}\theta_{Nav}(ij,b=0)}}{e^{\mathrm{i}\theta_{Nav}(ij,m)}} \tag{2.8}$$

for all $k$-space locations and all $b \neq 0$ scans. Note that the phase at the $b = 0$ scan includes the effect of the VOI matrix shift in image space of the water.

(d) **Filter & transform & frequency shift.** The phase corrected datasets can now be spatially Hanning filtered and zero padded from $12 \times 12$ tot $16 \times 16$, followed by a spatial and temporal Fourier transform depicted as

$$S_{xy,m}(f) = \mathcal{F}_t \Big\{ \mathcal{F}^{-1}_{ij} \left\{ s^{\{c\}}_{ij,m}(t) \cdot H_{ij} \right\} \Big\} \tag{2.9}$$

where $H_{ij}$ is the Hanning filter and $\mathcal{F}_t$ and $\mathcal{F}^{-1}_{ij}$ are the temporal forward and spatial inverse Fourier transform, respectively. To correct for $B_0$ inhomogeneity, the resulting spectra at each image location $(x, y)$ of each water suppressed scan are frequency shifted, as

$$S^{\{f\}}_{xy,m}(f) = S_{xy,m}(f - \Delta f_{xy}) \tag{2.10}$$

where the applied frequency shift ($\Delta f_{xy}$) is determined by the frequency offset from the center of the water peak in the non-water-suppressed scan.

(e) **Eddy current correction.** To correct for eddy currents induced by the gradients, the residual water signal in the FID is used. This is the residual water signal in the water-suppressed scan as the VAPOR pulse scheme was slightly deoptimized. The influence of the eddy currents can be modeled as a location and time specific added phase on the FID, matching

$$\phi(t) = \phi_{\mathrm{FID}}(t) \; + \; \phi_{\mathrm{EC}}(t) \tag{2.11}$$

where $\phi(t)$ is the measured phase, $\phi_{\mathrm{FID}}(t)$ is the phase of the FID if there were no eddy currents and $\phi_{\mathrm{EC}}(t)$ is the phase contribution of the eddy currents. With this model, the FID without eddy current influences can be calculated simply by subtracting the eddy current phase from the phase of the FID. This is equivalent to division of the measured FID by the complex unit vector with the estimated eddy current phase, as

$$s^{\{e\}}_{xy,m}(t) = s^{\{d\}}_{xy,m}(t) / e^{\mathrm{i}\phi_{\mathrm{EC}\ xy,m}(t)} \tag{2.12}$$

and results in the eddy current corrected FID: $s^{\{e\}}_{xy,m}(t)$. In order to apply equation (2.12) on the acquired data, the voxel-time specific phase contribution of the eddy currents needs to be estimated. This phase can be estimated from the residual water signal in the FID [3].

First, the spectra are transformed back to the temporal domain, retrieving the FIDs in image space. Next, linear prediction singular value decomposition (LPSVD) [16] is applied on the FIDs to isolate the water signal in the FIDs with its spectral components in a 1 ppm region around the water resonance. This results for each voxel, in the FID originating from the residual water: $s_{\mathrm{W}\ xy,m}(t)$ and is utilized as

$$\phi_{\mathrm{EC}\ xy,m}(t) = \angle s_{\mathrm{W}\ xy,m}(t) \tag{2.13}$$

to calculate $\phi_{\mathrm{EC}\ xy,m}(t)$. With the phase contribution of the eddy currents estimated, equation (2.12) can be applied on the data for each voxel $xy$ and each diffusion condition $m$.

(f) **Remove residual water resonance.** With the isolated water FIDs known from the LPSVD algorithm, the residual water resonance in the FID can be removed easily by extracting this from the eddy current corrected FID, as

$$s^{\{\mathrm{f}\}}_{xy,m}(t) = s^{\{\mathrm{e}\}}_{xy,m}(t)\ -\ s_{\mathrm{W}\ xy,m}(t) \tag{2.14}$$

resulting in the post-processed FID $s^{\{\mathrm{f}\}}_{xy,m}(t)$.

(g) **Export.** Now all the corrections have been applied on the measured data and the data has the correct format ($s^{\{\mathrm{f}\}}_{xy,m}(t)$), the 5 data matrices of the five scans can be exported to the *.SDAT*/ *.SPAR* Philips format for further spectral analysis.

### 2.2.3. Data Analysis

The spectral analysis is performed with LCModel [17]. LCModel produces an output table of metabolite quantities for each diffusion condition. In this table, the peak estimations and Cramér-Rao lower bounds (CRLB) are noted for each metabolite for each voxel $(x, y)$.

These tables are loaded into MATLAB where the $ADC$ can be calculated according to

$$ADC_{xy} = -\frac{\sum_{m=1}^{3} \ln\left(\frac{s_{xy,m}(b)}{s_{xy}(0)}\right)}{3\cdot b} \qquad \bigwedge \{b=0\} \notin \{m\} \tag{2.15}$$

for each metabolite of interest. If, however, the CRLB of the estimated signal of a metabolite in a voxel exceeds 10%, this value is discarded.

Here, $s_{xy,m}(b)$ is the metabolite signal intensity at image location $(x, y)$ and diffusion condition $m$ with corresponding $b$-value $(b > 0)$. Logically, $s_{xy}(0)$ is the signal intensity at image location $(x, y)$ without diffusion weighting. Once all the $ADC$s are calculated, the $ADC$-map is composed offering a new MR diagnostic tool. Such $ADC$-maps for the total NAA, Cr and Cho are shown in Figure 2.7.

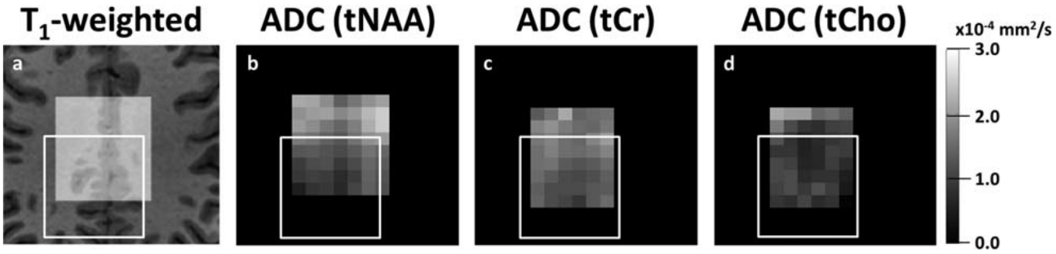

Figure 2.7: Metabolite $ADC$-maps with **(a)** T$_1$-weighted image as anatomical reference and **(b)**-**(d)** the corresponding the $ADC$-maps for tNAA, tCr, and tCho, respectively. The shifted VOI of the water resonance is framed in white [1].

# 3

# Scan Time Reduction Algorithms

In this chapter we will briefly discuss and consider possible methods to reduce the scan time of diffusion-weighted chemical shift imaging.

In MRI, each raw measurement (readout) contains the free induction decay echo under a phase encoding. All these readouts with their PEs contain the discretized spatial frequency components of the sample within the FOV and span $k$-space. By applying a multidimensional inverse spatial Fourier transform on $k$-space, an image (or volume) is obtained of the sample.

With MR spectroscopy, or chemical shift imaging (CSI), the readout contains the FID of a single location in $k$-space (PE), representing the time signal of the spectroscopy information. By applying a temporal Fourier transform in the $k$-space' time dimension and a multidimensional spatial inverse Fourier transform on the PE dimension, the spectroscopy dataset emerges.

However, since Nyquist states that the sampling frequency has to be twice the frequency of the highest frequency component in the signal and since in CSI every location in $k$-space (PE) requires a separate measurement, where each PE measurement cannot be accelerated due to the intrinsic properties of the tissue (as the $T_1$ time), it becomes quite a time-consuming task to fill $k$-space the Nyquist-way. In order to scan faster we aim to measure less PEs and still be able to reconstruct a full informative image.

## 3.1. Parallel Imaging

In parallel imaging (PI) the MR measurement setup consists of multiple parallel receive coils placed around the subject. This allows the FIDs to be measured simultaneously by the multiple parallel receive coils where each receive coil is characterized by its own spatial sensitivity. These multiple simultaneous measurements of the FID allow to sample under the Nyquist rate [5, 18, 19]. The aliasing due to the undersampling can be resolved using the prior knowledge of the specific undersampling pattern in $k$-space in combination with the parallel measurements. The two most common PI reconstruction algorithms are sensitivity encoding (SENSE) and generalized autocalibrating partial parallel acquisition (GRAPPA). GRAPPA [20] works as an interpolator on the missing PEs in $k$-space combining the data from the parallel receive coils and SENSE [21] unfolds and combines the aliased images from the parallel receive coils using the coil sensitivity maps (CSMs). The SENSE algorithm proved to be well applicable to spectroscopic imaging [22–24].

## 3.2. Compressed Sensing

Compressed sensing (CS) is a quite new signal processing technique which also allows to sample under the Nyquist rate. This technique is based on the observation that most modern signals/data (e.g. sound and images) can be compressed without any perceptual differences [25, 26]. Compressed sensing uses this compressibility property already in the acquisition to endeavour to efficiently measure only the principal data components and reconstruct according to $l_0$-norm minimization.

In order to apply CS on an MR dataset, the data must satisfy two conditions:

(a) the data must have a sparse representation in a known transform domain;

(b) in the data, the aliasing artifacts due to $k$-space undersampling must be incoherent in that transform domain.

Besides these two conditions on the data, CS itself requires a nonlinear reconstruction to enforce both sparsity of the data representation and consistency with the acquired data [6, 27]. As it turned out, CS was found well suited for MRI in the application of scan time reduction as well as noise reduction with the wavelet transform [28] as the most popular sparsifying transform. Also with spectroscopic imaging, compressed sensing already showed very promising results [29].

## 3.3. Parallel Imaging meets Compressed Sensing

Compressed sensing is, however, not an algorithm that combines the data from the multiple parallel receive coils, while most modern clinical scanners are equipped with a parallel receive coil system. To resolve this issue, PI-CS hybrids where developed to make CS applicable for the clinical MRI setting [30, 31]. Such hybrids are SPIRiT and ESPIRiT, where SPIRiT (iterative self-consistent parallel imaging reconstruction) [32] is an algorithm mainly based on GRAPPA and ESPIRiT (efficient L1-SPIRiT) [33] is its SENSE-incorporated extension.

Both PI-CS algorithms as well as CS are well described and implemented in the Berkeley Advanced Reconstruction Toolbox (BART) [34]. This toolbox has been introduced to the MRI community at the ISMRM 2016 Data Sampling and Image Reconstruction Workshop [35]. However, since SPIRiT and ESPIRiT are both autocalibrating imaging algorithms, they are presumably not flexible enough for the integration in the DW-CSI post-processing pipeline.

## 3.4. Compressed Sensing Parameter Mapping

In the last few years, CS has also been used as a tool for MR parameter mapping with its supplementary scan time reduction. In the case of $T_1$ and $T_2$-mapping, conventionally multiple full scans are required with different echo times (TEs) to depict the exponential $T_1$ recovery and $T_2$ decay, respectively. Compressed sensing, on the other hand, can preform the reconstruction and the estimation in one iterative scheme from the undersampled scans [36, 37]. Compressed sensing can achieve this by exploiting sparsity in the dataset through a custom overcomplete dictionary designed for parameter mapping. This has already been applied to $T_1$, $T_2$ and diffusion imaging [38, 39], however not yet to the diffusion of metabolites (DW-CSI).

**Conclusion** We believe that the iterative CS parameter estimation, pre-combined with the parallel coil combination according to the CSMs, will be the most flexible and appropriate method for accelerating DW-CSI. Compressed sensing parameter mapping and the CSMs will be explained further in the next chapter.

# 4

# Compressed Sensing Parameter Mapping for DW-CSI

In this chapter we will set forth our method to accelerate and analyze diffusion-weighted chemical shift imaging. First the differences in acquisition and initial post-processing will be explained, followed by the compressed sensing parameter mapping algorithm with its required elements.

## 4.1. Acquisition and Initial Post-Processing

In contrast to the DW-CSI acquisition of Subsection 2.2.1, we simulate to pseudo-random undersample the data in $k$-space, thus acquire less phase encodings in a predefined manner. This allows us to reduce the scan time of the DW-CSI scan. The PE undersampling pattern is different for each diffusion-weighted scan to enhance the incoherence in the aliasing artifacts. Only the first non-water-suppressed scan will contain all PEs used in the subsequent diffusion-weighted scans. To compensate for the loss in energy, the acquired PEs are divided by their corresponding $k$-space PE-probabilities as defined by the PE's probability density function. The design of the pseudo-random undersampling pattern will be further explained in Subsection 4.1.1. Furthermore, the diffusion gradients will be applied in one direction with three increasing $b$-values greater than zero, instead of one $b$-value in three perpendicular directions and the MR pulse scheme is set to only acquired the first echo.

In contrast to the post-processing of Subsection 2.2.2, we will combine the spectra from the parallel receive coils more accurate according to the Roemer reconstruction with the coil sensitivity maps instead of the $SNR$-phase weighted combination. This will be described in more detail in Subsection 4.1.2. The navigators measured by each receive coil, however, will still be combined according to step (a), since these signals are not spatially encoded.

A last deviation from the post-processing of Subsection 2.2.2 is in step (c). We no longer base the phase correction factor on the phase of the navigator of the water-suppressed $b = 0\ \mathrm{s/mm^2}$ scan, as depicted in the numerator of equation (2.8). Instead, we replace this numerator by the phase of the navigator of the non-water-suppressed scan. As these should give the same phase correction and will less restrict the DW-CSI acceleration, since all the navigators are required at each PE of the subsequent diffusion-weighted scans.

The rest of the operations on the data ((b), (d) - (f) of Subsection 2.2.2) will remain the same. Their outcome followed by a temporal inverse Fourier transform will result in a $[N_f \times N_x \times N_y \times N_m]$ multidimensional complex $k$-space matrix $\mathbf{s}$. The data at the acquired PE locations of spatially Fourier transformed matrix $\mathbf{s}$ will act as "ground truth measurements" or data consistency term.

Due to the applied operations in the image domain in the post-processing, the not-acquired PEs of $\mathbf{s}$ in $k$-space will not be empty or zero anymore. This data together with the data consistency term will serve as our initial input in the compressed sensing parameter mapping (CS-PM) algorithm. This algorithm will be set forth in the next section (Section 4.2).

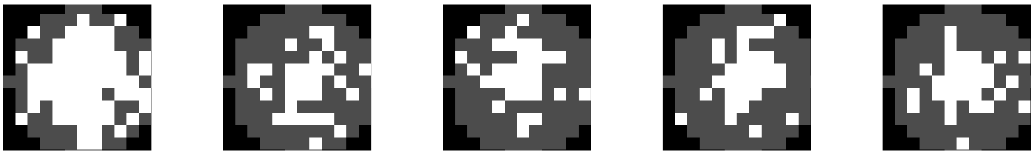

(a) MIP pattern $R_1 = 1.71$. (b) Unique pattern $R_2 = 3.65$. (c) Unique pattern $R_3 = 3.65$. (d) Unique pattern $R_4 = 3.65$. (e) Unique pattern $R_5 = 3.65$.

Figure 4.1: Phase encoding undersampling patterns generated with $R_{\text{net}} = 3.0$ on $12 \times 12$ $k$-space. The gray circular background highlights the full PE acquisition with circular $k$-space coverage.

### 4.1.1. Phase Encoding Undersampling Pattern

In several previous studies, a pseudo-random PE undersampling pattern has been applied. However, in most of these studies [18, 27, 30, 36, 40–42] an explanation of the generation of the undersampling pattern from a pre-described probability density function (PDF) was not clearly stated. We have implemented a fast and intuitive method to generate a PE undersampling pattern according to a given 2D PDF. This allows us to simulate a pseudo-random undersampled acquisition from a full acquired dataset.

According to the predefined acceleration factor $R$, the full acquisition pattern ($\text{PE}_{\text{full},ij}$) and its spatial dimensions $(N_i, N_j)$, a pseudo-random PE undersampling pattern is generated. First, from $R$ and $N_i, N_j$ a 2D spatial Gaussian PDF is calculated. With $\mu_{ij}$ in the center of $k$-space $((i, j) = (0,0))$ and $\sigma$ iteratively scaled such that

$$\sum_{ij} \text{PDF}_{ij} = \frac{1}{R} \sum_{ij} \text{PE}_{\text{full},ij} \qquad \bigwedge \text{PDF}_{0,0} = 1 \tag{4.1}$$

holds. Note that in this equation, the values of $\text{PDF}_{ij}$ on each point in $k$-space $(i, j)$ indicate the probability of that PE being acquired and the sum of $\text{PDF}_{ij}$ over all $k$-space must be equal to number of PEs in the full acquisition divided by the acceleration factor $R$. In this way, the loss in energy in the undersampled acquisition can be compensated as stated in the first paragraph of Section 4.1. Besides a Gaussian PDF, other distributions can also easily be incorporated.

Next, for the sampling pattern random values ($\mathcal{U}(0,1)$) are assigned to a grid with spatial dimensions $(N_i, N_j)$. To determine which of these grid points will result in an acquired PE, $\mathcal{T}$ is used as threshold on this grid. This threshold is set by the earlier calculated PDF and a scalar $\tau$, formulated as

$$\mathcal{T} = 1 - \text{PDF} + \tau \tag{4.2}$$

where this $\tau$ is iteratively scaled such that only $\frac{1}{R}\sum_{ij} \text{PE}_{\text{full},ij}$ PEs remain above the threshold. To enhance the incoherence of the aliasing artifacts, a different PE undersampling pattern is created for each diffusion-weighted scan [6]. If $k$-space data of a previous scan is required to correct for certain effects, as in DW-CSI post-processing 2.2.2, (c), the PE acquisition pattern of that scan can be generated by a projection over the PE patterns of the other scans, as a maximum intensity projection (MIP). To maintain the net acceleration factor $R$ as specified, the generation of the PDF, the PE sampling pattern of the unique scans and the MIP PE sampling pattern can again be iteratively scaled to comply with this $R$. Figure 4.1 visualizes an example set of PE undersampling patterns.

### 4.1.2. Roemer Reconstruction

To combine the data from the parallel receive coils more accurately than the $SNR$-phase coil combination of the DW-CSI post-processing of Subsection 2.2.2, step (a), the Roemer reconstruction is applied [43]. The Roemer reconstruction uses the coil sensitivity maps (CSMs) of the parallel receiver coils to combine the parallel measurements to the most optimal reconstructed image [43]. The Roemer reconstruction states that the acquired coil images ($\mathbf{S}$) are the linear combination of the desired full image ($\rho$) and the CSMs ($\mathbf{C}$). This is expressed voxel-wise in

$$\begin{bmatrix} s_{1,xy} \\ s_{2,xy} \\ \vdots \\ s_{N_c,xy} \end{bmatrix} = \begin{bmatrix} c_{1,xy} \\ c_{2,xy} \\ \vdots \\ c_{N_c,xy} \end{bmatrix} \rho_{xy} \tag{4.3}$$

where $N_\mathrm{c}$ depicts the number of parallel receive coils. These CSMs are estimated from a reference scan. This additional imaging scan has a wide FOV, a low resolution and takes approximately 1.5 minutes. The RF signals emitted by the object after excitation are received by the parallel receive coils as well as the body coil. The image from the body coil is assumed to have a homogeneous sensitivity [21].

By dividing the parallel receive coil images by both the body coil image and the coil noise variance, anatomical related structures are canceled out. The addition of the coil noise variance on the denominator prevents division by zero. The resulting images (CSMraw) contain the complex coil sensitivities and exploding background noise. The background noise can later on easily be discarded with the use of a binary object mask. This object mask can be determined from the body coil image. To eliminate the influence of the noise within the object, the raw coil sensitivity maps are smoothed. This smoothing can be performed by Gaussian filtering or by polynomial fitting. Polynomial fitting results in a more accurate CSM on the boundaries of the object however pays in its computational cost. Gaussian filtering will comply with the requirements of DW-CSI scans, since the selected VOI will always be planned within the object. After filtering, the smoothed CSM and its binary mask are rescaled to the FOV of the DW-CSI dataset. Eventually, the rescaled smoothed CSM and its binary mask are multiplied with each other. Figure 4.2 visualizes these steps for coil 12 as example.

For each voxel a CSM vector $\mathbf{C}_{xy}$ can be composed as

$$\mathbf{C}_{xy} = \left[c_{1,xy} \quad c_{2,xy} \quad \dots \quad c_{N_\mathrm{c},xy}\right]^T \tag{4.4}$$

that indicates the spatial sensitivity of each receive coil on that voxel. With this vector, the spectra measured by each receive coil ($\mathbf{S}^{\{0\}}_{xy,m}(f)$) can be combined in image space with the best linear unbiased estimator (BLUE) [44], given by

$$S^{\{a\}}_{xy,m}(f) = \left(\mathbf{C}^H_{xy}\Xi^{-1}\mathbf{C}_{xy}\right)^{-1}\mathbf{C}^H_{xy}\Xi^{-1}\;\mathbf{S}^{\{0\}}_{xy,m}(f) \tag{4.5}$$

where $\mathbf{S}^{\{0\}}_{xy,m}(f) \in \mathbb{C}^{N_\mathrm{c}\times 1}$. We assume that the incoherent noise-like artifacts originating from the PE undersampling pattern, will remain incoherent and noise-like after applying this linear reconstruction. In equation (4.5), $\Xi \in \mathbb{C}^{N_\mathrm{c}\times N_\mathrm{c}}$ is the parallel coil noise covariance matrix and is estimated from the voxel outside the dilated object mask ($\boldsymbol{\Gamma} \in \mathbb{C}^{N_\mathrm{vxls}\times N_\mathrm{c}}$) in the raw sensitivity maps as in

$$\Xi = \mathrm{E}\left[(\boldsymbol{\Gamma} - \mathrm{E}[\boldsymbol{\Gamma}])(\boldsymbol{\Gamma} - \mathrm{E}[\boldsymbol{\Gamma}])^H\right] \tag{4.6}$$

where the noise is assumed to be Gaussian.

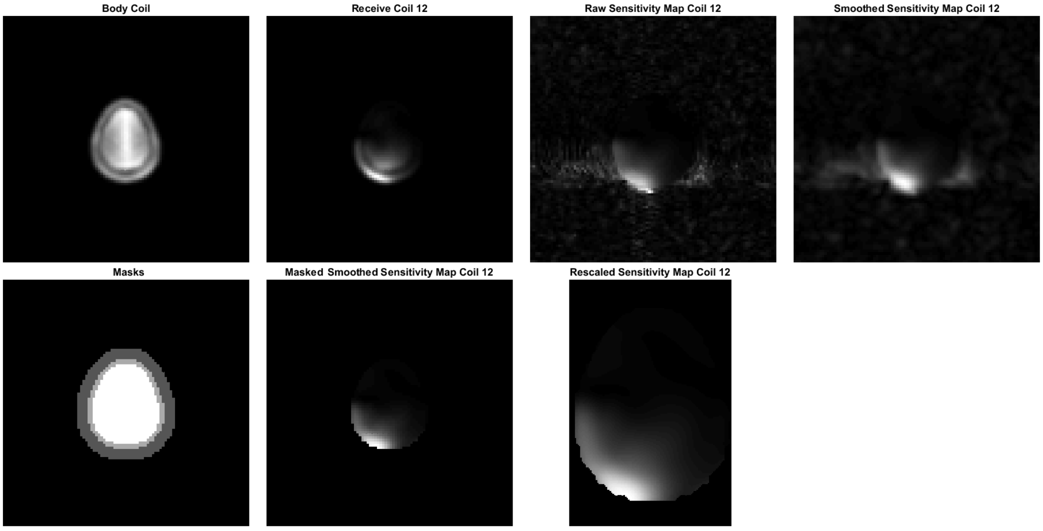

Figure 4.2: Construction of coil sensitivity maps with Gaussian filtering.
The bottom left figure visualizes 3 object masks: dilated, normal and eroded. Coil 12 is depicted as example.

## 4.2. Reconstruction

After the data is acquired according to a PE undersampling pattern (Subsection 4.1.1); from the separate coil measurements: the FIDs are combined according to the CSMs (Subsection 4.1.2) and the navigators are combined according to their $SNR$ and phase (Subsection 2.2.2, step (a)); and post-processing steps (b) - (f) of Subsection 2.2.2 have been applied on the data, the resulting $s^{\{f\}}_{xy,m}(t)$ is temporally Fourier transformed and stored in matrix $\mathbf{s} \in \mathbb{C}^{N_f \times N_x \times N_y \times N_m}$.

On matrix **s**, the signal of the metabolite of interest is isolated on its resonance frequency. Subsequently, the compressed sensing parameter mapping technique is applied to reconstruct the missing $k$-space data and the metabolites diffusion properties are extracted. This will be explained in the following subsections.

### 4.2.1. Compressed Sensing in MRI

As stated earlier in Section 3.2, compressed sensing is a technique that allows to sample under the Nyquist rate and uses an inverse problem optimization to reconstruct the missing samples. Two requirements on the MR dataset need to be satisfied in order to apply CS:

(a) the data must have a sparse representation in a known transform domain;

(b) in the data, the aliasing artifacts due to $k$-space undersampling must be incoherent in that transform domain.

In theory, CS uses the $l_0$-norm minimization to solve the optimization mathematically formulated as

$$\underset{\mathbf{x}}{\text{minimize}}\ \|\boldsymbol{\gamma}\|_0, \text{ subject to } \|\mathbf{y} - \boldsymbol{\Phi}\mathbf{x}\|_2 \leq \epsilon \tag{4.7}$$

and describes the inverse problem for finding the optimal solution for signal **x**, where $\mathbf{x} = \boldsymbol{\Psi}\boldsymbol{\gamma}$ with $\boldsymbol{\gamma}$ the sparse representation, $\boldsymbol{\Psi}$ the sparsifying transform, **y** the measurement vector, $\boldsymbol{\Phi}$ the measurement matrix and $\epsilon$ the noise related error [36].

However, since this $l_0$ minimization problem is not convex, finding a solution numerically is intractable. Therefore, as convex approximation, the $l_1$-norm inversion is generally used. It has been shown that this will result in approximately the same solution as the $l_0$-norm if the result is sufficiently sparse [25]. The method used to solve this $l_0$ minimization problem in this study will be set forth in Subsection 4.2.5. The estimated sparsity domain will be that of the diffusion parameter: $ADC$.

Numerically, CS with its $l_1$-norm minimization, can by performed iteratively. In this iterative scheme the signals have a representation in the measurement domain and a sparse domain. This measurement domain can be, for example, $k$-space. If the signal to be recovered/estimated is not naturally sparse, the measurements in that same signal domain will have to be transformed to a sparse domain by, for example, a wavelet transformation [45]. In this sparse domain a soft-threshold can be applied to extract the significant signal components from the noise-like aliasing artifacts [6, 29, 30]. In this way, the absolute sum of the elements in $\boldsymbol{\gamma}$ is minimized: $l_1$-norm minimization. This soft-threshold function is defined as

$$\mathcal{T}_s(\boldsymbol{\gamma}, \lambda) = \begin{cases} \dfrac{(|\boldsymbol{\gamma}| - \lambda)}{|\boldsymbol{\gamma}|}\boldsymbol{\gamma} & \text{if } |\boldsymbol{\gamma}| > \lambda \\ 0 & \text{if } |\boldsymbol{\gamma}| \leq \lambda \end{cases} \tag{4.8}$$

where $\lambda$ is the threshold level. Subsequently, the resulting thresholded, denoised data is transformed back to the measurement domain and the actual measurements are forced on this dataset as the data consistency term. The initially missing samples (zero-valued samples) in the measurement domain will now contain nonzero values. Thus, in this manner the data is polished with each iteration, estimating the missing samples in the measurement domain. This iterative process continues until the $l_2$-norm of the difference between each iteration of the measurement domain becomes smaller than the estimated noise level. Figure 4.3 visualizes this iterative CS reconstruction for an MRI dataset with wavelets as sparsifying representation.

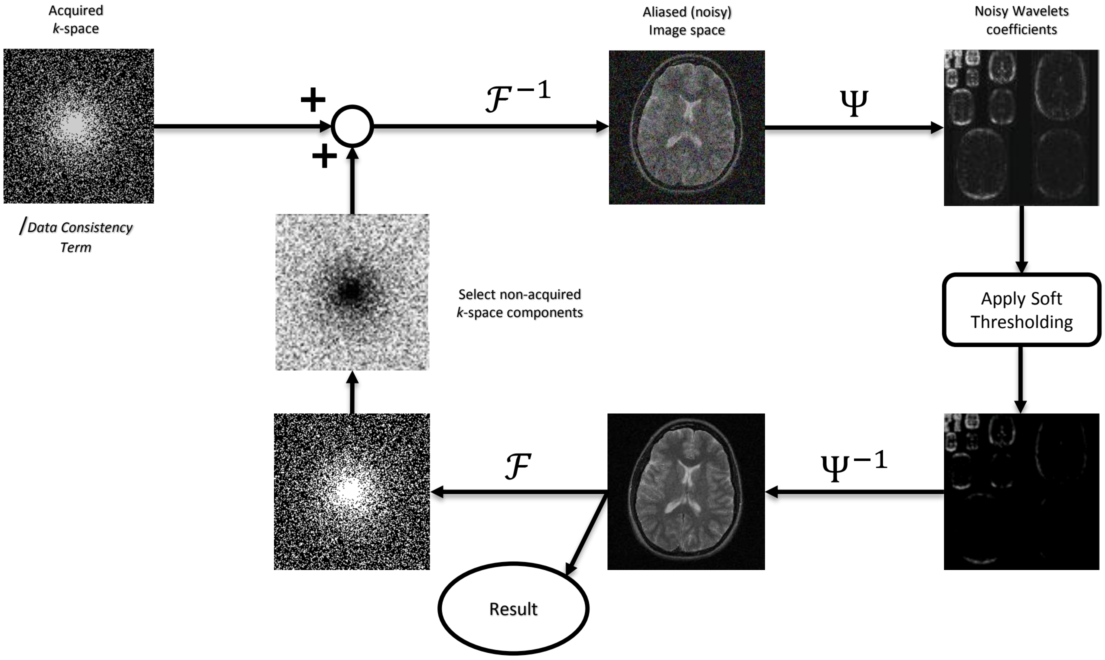

Figure 4.3: Iterative compressed sensing reconstruction scheme visualized for MRI data. Starting with the undersampled $k$-space data. This data is transformed to the image domain and, subsequently, the wavelet domain where the soft-threshold is applied for denoising. Next, the thresholded data is transformed back to the image domain and to $k$-space. In the new estimated $k$-space the initially non-acquired data is selected and combined with the data consistency term. This iterative scheme continues until the reconstruction converges.

### 4.2.2. *k-p* space

In order to use CS for parameter mapping, Doneva et al. (2010) [36] introduced a generalized framework based on the model $f(p;\theta)$ [36]. Here, $\theta$ is our parameter of interest and can be spatially estimated with the information of the multiple scans with each a different encoding parameter $p$. In the case of DW-CSI, $\theta$ resembles the $ADC$ and $p$ the diffusion condition $m$ with its $b$-value.

The measured data is collected in a measurement space called $k$-$p$ space. Figure 4.4 shows an example of such a $k$-$p$ space for $T_1$ and $T_2$-mapping. Here, the readouts are stored in the $k_x$ dimension under their PEs in $k_y$. The multiple scans with different encoding parameter setting are collected in the $p$ dimension.

In our implementation, $k$-$p$ space will be constructed from matrix $\mathbf{s}$. To estimate the signal contribution of the metabolite of interest, pole estimation is applied on the FID of each voxel of $\mathbf{s}$ by LPSVD [16]. The resulting magnitude of the estimated pole is then equal to its energy contribution in the spectrum. For the metabolite NAA, which has its resonance frequency at 2.0 ppm, all estimated poles within a range of $2.0 \pm 0.25$ ppm are added up and form the scalar complex value of that voxel in $\mathbf{S} \in \mathbb{C}^{N_x \times N_y \times N_m}$. Subsequent, $\mathbf{S}$ is spatial Fourier transformed creating the $k$-$p$ space matrix $\mathbf{y}$.

### 4.2.3. Sparsity

In compressed sensing MRI, a wavelet transformation [45] is the most common sparsifying transformation. However, if we design a custom parametric model-based sparsifying transformation, the parameter to be estimated can be directly read from this sparse domain. This model-based transform is the dictionary [36] together with the orthogonal matching pursuit (OMP) algorithm. The dictionary $\boldsymbol{\Psi}$ forms the translation between the sparse parameter domain $\boldsymbol{\gamma}$ and the measurements in image space $\mathbf{x}$. Here, $\mathbf{x}$ is the spatial inverse Fourier transform of the measurements $\mathbf{y}$. The design of the dictionary and the explanation of OMP are further described in Subsections 4.2.4 and 4.2.5, respectively.

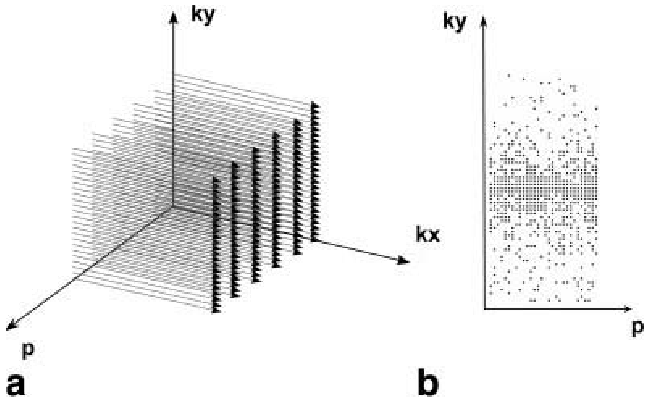

Figure 4.4: Imaging example of data acquisition in Cartesian $k$-$p$ space, with the readout, phase encoding and parameter directions in $k_x$, $k_y$ and $p$, respectively [36]. **(a)** Conventional full sampling for each imposed parameter value $p$. **(b)** Pseudo-random undersampling in $k$-$p$ space for compressed sensing (readout is orthogonal to the drawing plane).

### 4.2.4. Dictionary

The dictionary $\mathbf{\Psi}$ serves as model-based sparsity transform and is an overcomplete collection of discrete-parameter signal prototypes (atoms) [36]. It is important that this dictionary is overcomplete to enforce sparsity. Starting with a generalized exponential model from Doneva et al. (2010) [36] formulated as

$$M(p) = \alpha + \beta\, e^{-p/\tau} \tag{4.9}$$

and with equations (2.3) and (2.4) of Subsection 2.2.1, the generalized model can be rewritten to

$$S_{xy}(b) = S_{xy}(0)\, e^{-b\ ADC} \tag{4.10}$$

where $S_{xy}$ represents the metabolites signal in voxel $(x, y)$ under diffusion condition $b$. The parameter we would like to estimate is the $ADC$. With this model and the expected range of $ADC$, the dictionary is composed as

$$\begin{aligned}\mathbf{\Psi} &= \begin{bmatrix} e^{-b_1 ADC_1} & e^{-b_1 ADC_2} & \dots & e^{-b_1 ADC_n} \\ e^{-b_2 ADC_1} & e^{-b_2 ADC_2} & \dots & e^{-b_2 ADC_n} \\ \vdots & \vdots & \ddots & \vdots \\ e^{-b_m ADC_1} & e^{-b_m ADC_2} & \dots & e^{-b_m ADC_n} \end{bmatrix} \\ &= \begin{bmatrix} \mathbf{a}_1 & \mathbf{a}_2 & \dots & \mathbf{a}_n \end{bmatrix}\end{aligned} \tag{4.11}$$

whereby, each column in $\mathbf{\Psi}$ represents an atom, $\mathbf{a}$, of length $m$ (number of scans), $n$ indicates the number of atoms and determines the resolution in the parameter range and provides the overcompleteness of the dictionary. The $ADC$ values range linear from $ADC_1 = 0$ to $ADC_n = 7.0 \cdot 10^{-3}$ mm$^2$/s. The maximum $ADC$-value was chosen at approximately two times the maximum expected $ADC$ of water in the human brain [46]. The number of atoms is set at 10,000.

With this configuration the dictionary has a precision defined by

$$\psi = \frac{ADC_n - ADC_1}{n} \tag{4.12}$$

resulting in $\psi = 7.0 \cdot 10^{-7}$ mm$^2$/s. Currently the atoms of $\mathbf{\Psi}$ do not have equal norm and this leads to a bias in the parameter mapping. To resolve this, all the columns of $\mathbf{\Psi}$ are normalized as

$$\widehat{\mathbf{\Psi}} = \begin{bmatrix} \frac{\mathbf{a}_1}{\|\mathbf{a}_1\|} & \frac{\mathbf{a}_2}{\|\mathbf{a}_2\|} & \cdots & \frac{\mathbf{a}_n}{\|\mathbf{a}_n\|} \end{bmatrix} \tag{4.13}$$

resulting in $\widehat{\mathbf{\Psi}}$ which is applied in the parameter mapping. Figure 4.5 shows a visual representation of matrices $\mathbf{\Psi}$ and $\widehat{\mathbf{\Psi}}$. As an optional step, wavelets or finite differences can be applied to further sparsify the image domain [36] and to act as regularization.

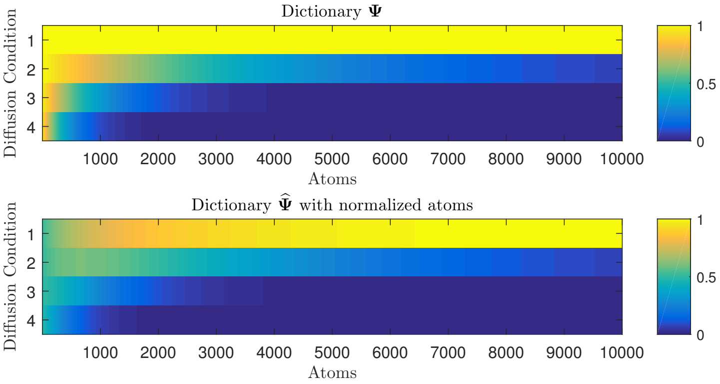

Figure 4.5: Dictionary matrices $\mathbf{\Psi}$ and $\widehat{\mathbf{\Psi}}$ visualized for diffusion conditions $b = \{0,\ 382,\ 1531,\ 3445\}$ in s/mm$^2$.

### 4.2.5. Orthogonal Matching Pursuit

Orthogonal matching pursuit [47, 48] is a recursive search algorithm which tries to solve the inverse problem of the linear system depicted as

$$\widehat{\mathbf{\Psi}}\,\boldsymbol{\gamma} = \mathbf{x} \tag{4.14}$$

where $\mathbf{x} \in \mathbb{R}^{m\times 1}$ is our given signal and $\widehat{\mathbf{\Psi}} \in \mathbb{R}^{m\times n}$ is the non-orthogonal and overcomplete dictionary constructed of normalized signal prototypes (atoms $\hat{\mathbf{a}}$). The vector $\boldsymbol{\gamma} \in \mathbb{R}^{n\times 1}$ is the desired sparse representation and indicates the linear combination of atoms of $\widehat{\mathbf{\Psi}}$ to reconstruct $\mathbf{x}$. This can be reformulated as an optimization problem stated as

$$\underset{\boldsymbol{\gamma}}{\text{minimize}}\ \|\mathbf{x} - \widehat{\mathbf{\Psi}}\boldsymbol{\gamma}\|_2,\ \text{subject to}\ \|\boldsymbol{\gamma}\|_0 \le \mathcal{K} \tag{4.15}$$

where this mathematical expression is actually telling that a $\boldsymbol{\gamma}$ should be found that minimizes the error produced in the model above and at the same time where $\boldsymbol{\gamma}$ should be as sparse as possible: at most $\mathcal{K}$ nonzero entries. Orthogonal matching pursuit can do this by calculating all the inner products between the signal $\mathbf{x}$ and all the dictionaries atoms $\hat{\mathbf{a}}$. The highest inner product (highest correlation) is stored in $\boldsymbol{\gamma}$ at the index of the corresponding atom. Subsequently, a residual perpendicular to the space spanned by the set of selected atoms is calculated. In this way, signal $\mathbf{x}$ is decomposed in a linear combination of orthogonal atoms.

If only the first found atom is used ($\mathcal{K} = 1$), the OMP algorithm will produce the same outcome as basic matching pursuit. This will be in fact the case for our reconstruction since we assume only one $ADC$-value per voxel.

### 4.2.6. Regularization

The CS-PM algorithm discussed up till now only reconstructs the data voxel-wise in the parameter direction. This implies that the spatial smoothness of CSI images in the image domain might not be preserved. With operations in the image domain such as wavelets or finite differences to further sparsify the data, as proposed by Doneva et al. [36], the coherence in the image domain can be preserved. However, these two methods are not presumed appropriate methods for the CSI images considering the size and data density. These two arguments are the main reason wavelets cannot act as a proper sparsification method. Finite differences could most likely not sparsify the image within the VOI, considering the shape of the CSI signal and its large voxel size.

Instead of wavelets or finite differences, we propose a simple 2D low-pass filter that is applied in $k$-space after the OMP estimation and before the data consistency term is applied. This low-pass filter, or regularization filter, $\mathbf{H}$ is defined as a 2D periodic generalized Hamming filter with an amplitude at the center of $k$-space of $h_{\mathrm{c}}$ and an amplitude at the periphery of $k$-space of $h_{\mathrm{p}}$, where $0 < h_{\mathrm{c}} < 1$ and $0 < h_{\mathrm{p}} < h_{\mathrm{c}}$. The overall attenuation from the $h_{\mathrm{c}}$ coefficient at the center of $k$-space will slow down the reconstruction, but will constrain the chance of divergence of the data. The slightly lower coefficients at the periphery of $k$-space ($h_{\mathrm{p}}$) will induce a coupling of the voxels in the image domain without enforcing to much blurring. The values of $h_{\mathrm{c}}$ and $h_{\mathrm{p}}$ were empirically determined to 0.9 and 0.65, respectively.

### 4.2.7. Reconstruction Algorithm

With the measured and processed data collected in $k$-$p$ space and a proper dictionary defined, the CS-PM iterative algorithm can be applied.

First, the data consistency term $\mathbf{y}|_{\text{acq}}$ is assigned as:

$$y_{ij,m}|_{\text{acq}} = \begin{cases} y_{ij,m} & \text{if } (ij,m) \text{ is acquired PE,} \\ 0 & \text{otherwise.} \end{cases} \tag{4.16}$$

Next, the iterative process is initiated with $\hat{\mathbf{y}}^{(0)} = \mathbf{y}$ and $\mathbf{x}^{(0)} = \mathbf{0}$.
For each iteration $i = \{1,\ 2,\ \dots,\ i_{\max}\}$:

1. Fourier transform $\hat{\mathbf{y}}^{(i-1)}$ to image space:

$$\mathbf{x}^{(i)} = \mathcal{F}_{ij}^{-1}\left\{\, \hat{\mathbf{y}}^{(i-1)} \,\right\} \tag{4.17}$$

2. For each voxel, transform the magnitudes of $\mathbf{x}_{xy}^{(i)}$ to sparse parameter domain using OMP with $\mathcal{K} = 1$:

$$\boldsymbol{\gamma}_{xy}^{(i)} = \text{OMP}\left( \left|\mathbf{x}_{xy}^{(i)}\right|,\ \widehat{\boldsymbol{\Psi}},\ \mathcal{K} \right) \tag{4.18}$$

3. Transform of each voxel $\boldsymbol{\gamma}$ back to image space:

$$\left|\hat{\mathbf{x}}_{xy}^{(i)}\right| = \widehat{\boldsymbol{\Psi}} \cdot \boldsymbol{\gamma}_{xy}^{(i)} \tag{4.19}$$

4. Add original phase to $\hat{\mathbf{x}}_{xy}^{(i)}$:

$$\hat{\mathbf{x}}_{xy}^{(i)} = \left|\hat{\mathbf{x}}_{xy}^{(i)}\right| \cdot e^{\mathrm{i}\cdot\angle \mathbf{x}_{xy}^{(i)}} \tag{4.20}$$

5. Fourier transform $\hat{\mathbf{x}}^{(i)}$ to $k$-$p$ space:

$$\tilde{\mathbf{y}}^{(i)} = \mathcal{F}_{xy}\left\{\, \hat{\mathbf{x}}^{(i)} \,\right\} \tag{4.21}$$

6. Low-pass filter $\tilde{\mathbf{y}}^{(i)}$ to restrict divergence and maintain spatial smoothness:

$$\hat{\mathbf{y}}^{(i)} = \tilde{\mathbf{y}}^{(i)} \cdot \mathbf{H} \tag{4.22}$$

7. Enforce data consistency term $\mathbf{y}|_{\text{acq}}$ on $\hat{\mathbf{y}}^{(i)}$:

$$\hat{\mathbf{y}}^{(i)} = \begin{cases} \mathbf{y}|_{\text{acq}} & \text{if PE is acquired,} \\ \hat{\mathbf{y}}^{(i)} & \text{otherwise.} \end{cases} \tag{4.23}$$

8. Repeat steps 1 - 7, until change in energy in image space becomes smaller than $\epsilon$ or when the maximum iteration number is reached:

$$\frac{\left\|\mathbf{x}^{(i)} - \mathbf{x}^{(i-1)}\right\|_2}{\left\|\mathbf{x}^{(i)}\right\|_2} < \epsilon \qquad \bigvee \quad i > i_{\max} \tag{4.24}$$

The values of $\epsilon$ and $i_{\max}$ were set empirically to $1^{-5}$ and 500, respectively.

At the end of this CS-PM iterative algorithm, the index of the nonzero entry in the sparse vector $\boldsymbol{\gamma}_{xy}^{(i)}$ indicates the eventual estimated *ADC* value of the metabolite of interest for that voxel $(x, y)$.

# 5

# Results & Evaluation

In this chapter we will test and discuss the compressed sensing parameter mapping algorithm on diffusion-weighted chemical shift imaging. First we will present our synthetic and acquired data. This data is subsequently used to evaluate the subelements of our CS-PM and the performance of the complete algorithm.

## 5.1. Data

To design and evaluate the compressed sensing parameter mapping algorithm, synthetic data has been generated and actual MR diffusion brain data has been acquired.

### 5.1.1. Synthetic Data

The synthetic dataset of four CSI scans has been designed with two principal components: the *ADC*-map and the $b = 0$ CSI scan, both in an FOV of $16 \times 16$ voxels. The *ADC*-map is designed with its *ADC* values ranging from $0.54 \cdot 10^{-3}$ to $1.37 \cdot 10^{-3}$ $\text{mm}^2/\text{s}$ in a diagonal infinity $(\infty)$ figure as visualized in Figure 5.1b.

The $b = 0$ CSI scan is designed as the magnitude of a 2D Hamming window multiplied with Gaussian noise describes as $\mathcal{N}_{\text{VOI}}\left(1, {}^{1}/_{10}{}^{2}\right)$ within and $\mathcal{N}_{\overline{\text{VOI}}}\left(0, {}^{1}/_{10}{}^{2}\right)$ outside the VOI. The VOI is defined as the rectangular region in the FOV spanning the voxels $x_{\text{VOI}} \in [4,\ 13]$ and $y_{\text{VOI}} \in [5,\ 12]$. This simulates the major CSI signal originating from the PRESS excited volume in the larger phase encoded FOV.

Subsequently, three $b > 0$ CSI scans are calculated according to the exponential decay model as described earlier in equation (2.3). The applied $b$-values are $b = \{0,\ 382,\ 1531,\ 3445\}$ in $\text{s}/\text{mm}^2$. This results in the CSI images shown in Figure 5.1a.

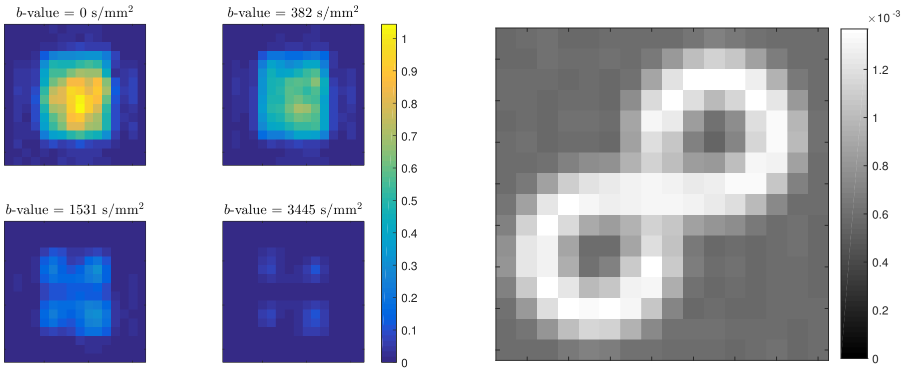

(a) Synthetic CSI images [a.u.].

(b) Synthetic *ADC*-map [$\text{mm}^2/\text{s}$].

Figure 5.1: Synthetic diffusion-weighted chemical shift imaging dataset.

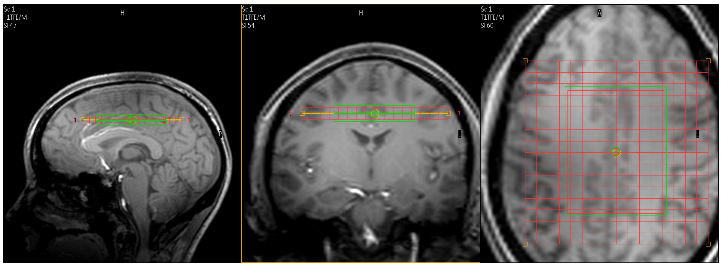

Figure 5.2: A plan of a DW-CSI scan slightly superior to the corpus callosum. The FOV (red) and the VOI (green) are visualized on top of the anatomical survey scan in sagittal, coronal and transverse view.

### 5.1.2. Acquired Data

The acquired in-vivo data was obtained from two healthy volunteers at Leiden University Medical Center (LUMC). The MR acquisitions were performed on a 7T Achieva Philips whole-body MRI scanner with a 32-channel Nova Medical head coil. The total set of acquired scans for each dataset is composed of:

1. an anatomical 3D survey scan, for further scan planning;
2. a reference scan, for the CSMs;
   (exported as: *.DATA*/*.LIST* & *.PAR*/*.REC*)
3. an anatomical 3D $T_1$-weighted scan, as anatomical reference later on;
   (exported as: *.DICOM*)
4. a non-PE-reduced DW-CSI scan, consisting of the five subscans:
   (exported as: *.DATA*/*.LIST* & *.PAR*/*.REC*)
   - one CSI scan without water suppression,
     without an applied diffusion condition ($b = 0$ s/mm$^2$);
   - one CSI scan with water suppression,
     without an applied diffusion condition ($b = 0$ s/mm$^2$);
   - three CSI scan with water suppression,
     with increasing diffusion conditions in a fixed diffusion direction ($b > 0$ s/mm$^2$).

Besides these scans, the examcard is also exported, providing a retrospective overview of all scan settings. Figure 5.2 shows the plan of a DW-CSI scan overlaid on the anatomical survey scan.

One dataset was scanned without and one with water suppression where the water ($H_2O$) and N-acetylaspartate (NAA) signal are examined, respectively. Figure 5.3 shows the CSI images of these acquired datasets in full acquisition after the conventional post-processing. These and all subsequent CSI images and *ADC*-maps will have the anterior to posterior direction on the vertical axis and the right to left direction on the horizontal axis with most anterior-right voxel on the top left of the images. As proof of concept and due to *SNR* considerations, we shall for most results only focus on the performance on the $H_2O$ scan.

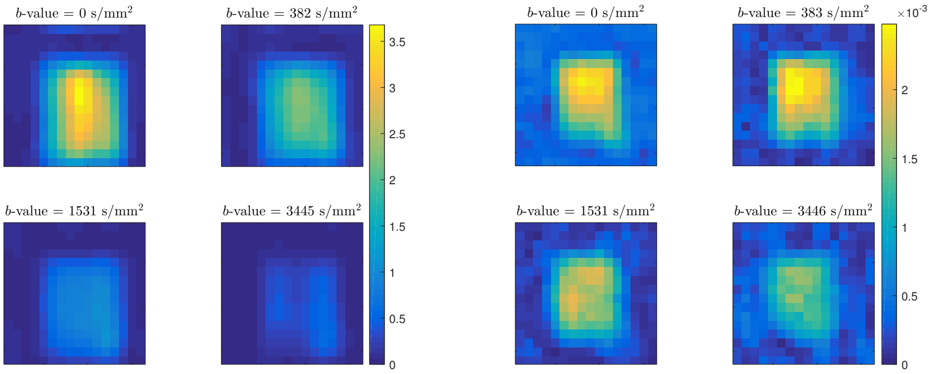

(a) Acquired $H_2O$ DW-CSI images [a.u.]. (b) Acquired NAA DW-CSI images [a.u.].

Figure 5.3: Full acquired diffusion-weighted CSI images after post-processing.

## 5.2. Results

To evaluate the CS-PM algorithm, first multiple sub-elements are evaluated on its performance on the $H_2O$ scan before examining the whole algorithm. The evaluations are mainly based on visual examinations as well as numerical evaluations on the resulting normalized root mean square error (NRMSE) [44], when instructive. The NRMSE is defined as

$$\mathrm{NRMSE}(\hat{\theta}) = \frac{1}{\theta_{\max} - \theta_{\min}} \sqrt{\frac{1}{n} \sum_{i=1}^{n} \left(\hat{\theta}_i - \theta_i\right)^2} \tag{5.1}$$

where $\hat{\theta}$ represents the estimation of the parameter of interest $\theta$. The normalization in the NRMSE is achieved by dividing the root mean square error by the range of $\theta$. The estimated $ADC$-maps are evaluated only within the VOI since this volume provides the main signal of interest as it is excited by the PRESS sequence.

In the following analyses, we will refer to the acquired datasets with full circular $k$-space coverage, simply as the full acquisition. Moreover, the data from the parallel receive coils is combined with the conventional $SNR$-phase combination of post-processing step (a) of Subsection 2.2.2, unless explicit described otherwise.

All analyses were performed in MATLAB on a laptop (CPU i5-5200U@2.20GHz, 16.00GB RAM) or more equipped desktop computer.

### 5.2.1. Dictionary

The completeness of the dictionary was evaluated by verifying that the parameter-image space can be spanned by the column space of the dictionary, mathematically expressed by: $|\mathbf{X}| \subset \mathcal{C}\left(\hat{\mathbf{\Psi}}\right)$. This was investigated by finding the best linear orthogonal combination of atoms with OMP ($\mathcal{K} = 4$) to span $|\mathbf{X}|$. The full acquired datasets of the $H_2O$ and the NAA scans were used to test this. The result for the $H_2O$ scan is visualized in Figure 5.4. As can be seen in Figure 5.4b, the resulting error between the signal $|\mathbf{X}|$ and its estimation by OMP $|\hat{\mathbf{X}}|$ is in the order of $10^{-14}$, with as error mean $\mu = -3.36 \cdot 10^{-18}$ and standard deviation $\sigma = 1.54 \cdot 10^{-15}$. The dictionary evaluation on the NAA scan showed similar results with: $\mu = -3.28 \cdot 10^{-19}$ and $\sigma = 4.80 \cdot 10^{-18}$. With these results we can conclude that the dictionary can sufficiently span the signals to be estimated.

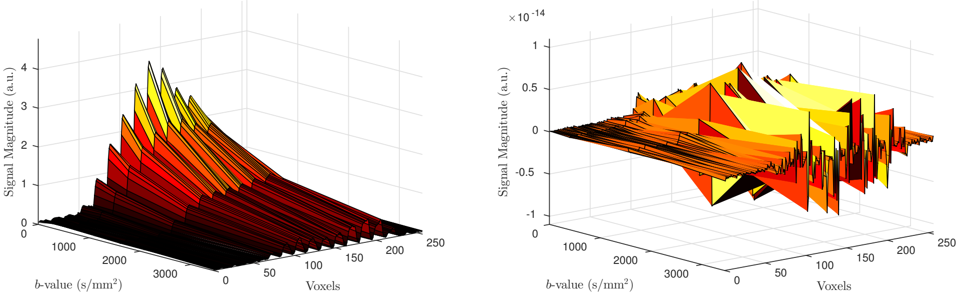

(a) Parameter-Image space of $|\mathbf{x}^{(1)}|$ of the full $H_2O$ acquisition.

(b) Parameter-Image space of residual $|\mathbf{x}^{(1)}| - |\hat{\mathbf{x}}^{(1)}|$ of the full $H_2O$ acquisition with $\mathcal{K} = 4$ in OMP.

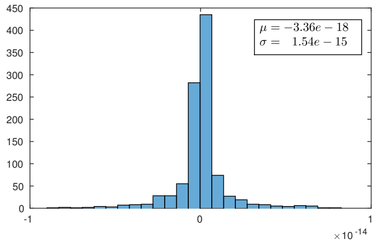

(c) Histogram of all data points in Figure 5.4b.

Figure 5.4: Dictionary validation.

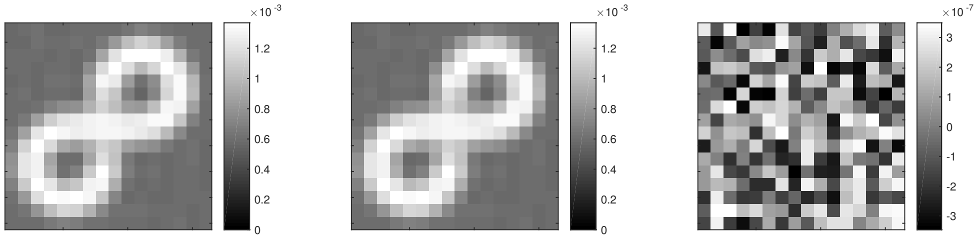

(a) Benchmark *ADC*-map. (b) Estimated*ADC*-map. (c) Difference.

Figure 5.5: Parameter mapping validation with synthetic data [mm$^2$/s].
**(a)** synthetic benchmark; **(b)** direct PM estimation and **(c)** their difference.

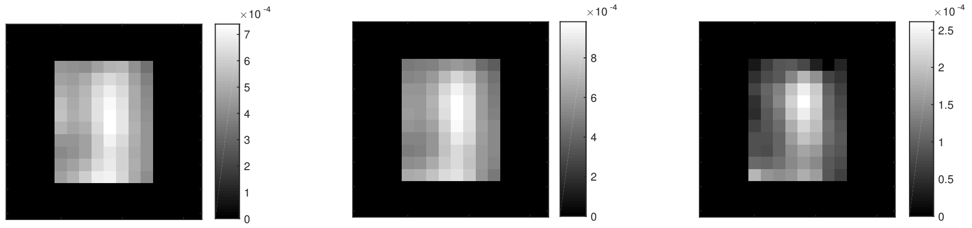

(a) Benchmark *ADC*-map (LUMC). (b) Estimated*ADC*-map. (c) Difference.

Figure 5.6: Direct parameter mapping on full $H_2O$ scan [mm$^2$/s].
**(a)** LUMC benchmark; **(b)** *SNR*-phase combination and **(c)** their difference.

### 5.2.2. Parameter Mapping

The accuracy of the parameter mapping was evaluated with the synthetic data. By direct parameter estimation with OMP ($\mathcal{K} = 1$), an *ADC*-map was estimated. The difference between the synthetic benchmark *ADC*-map and the estimated *ADC*-map was found to be within the precision of the dictionary as $\psi = 7.0 \cdot 10^{-7}$, as can be reviewed in Figure 5.5.

The direct parameter mapping was also applied on the full acquired $H_2O$ dataset. As can be observed in Figure 5.6, the result of the direct parameter mapping resembles the benchmark *ADC*-map quite well. The difference made by the OMP estimation ($|\hat{\mathbf{x}}^{(1)}|$) and the measured data ($|\mathbf{x}^{(1)}|$) can be characterized by a Gaussian distribution ($\mu = 8.3 \cdot 10^{-3}$ and $\sigma = 5.8 \cdot 10^{-3}$). The benchmark *ADC*-map in Figure 5.6a was provided by the LUMC. The two major differences that can be observed are a slight amplitude overestimation and two voxels on the anatomic mid-right side of the VOI. Considering the small error made by the OMP estimation on the data, the significant visual resemblance between the LUMC benchmark and the parameter mapping result from the same measured and processed input data, we argue that our estimated *ADC*-map is equally informative.

As a more appropriate comparison, the direct PM estimation will function as benchmark for the succeeding evaluations.

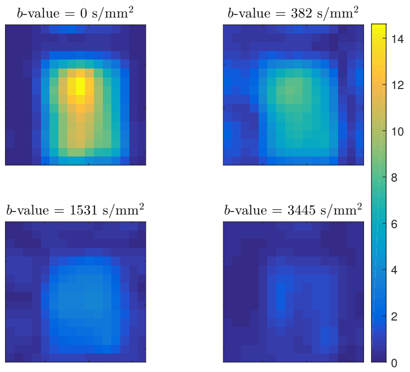

Figure 5.7: Acquired $H_2O$ CSI images after post-processing with Roemer reconstruction [a.u.].

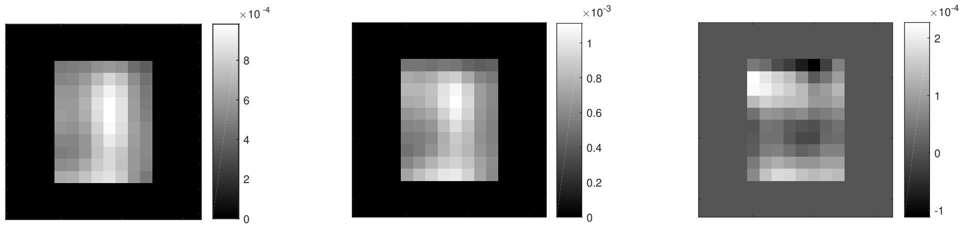

(a) Benchmark $ADC$-map (PM). (b) Estimated$ADC$-map. (c) Difference.

Figure 5.8: Direct parameter mapping on full $H_2O$ scan [$mm^2/s$].
**(a)** $SNR$-phase combination; **(b)** Roemer reconstruction and **(c)** their difference.

### 5.2.3. Roemer Reconstruction

The Roemer reconstruction has already proven its value in the MR field to combine the data from the parallel receive coils with their CSMs in the past 26 years [18, 19, 21, 43]. Thus, it would be unnecessary to validate every aspect of this reconstruction. In fact, the use of the CSMs to combine the parallel coil data should perform better than the LUMC benchmark which was calculated by the $SNR$-phase coil combination. In this evaluation, the result of the Roemer reconstruction on the full $H_2O$ datasets is examined.

The CSI result of the Roemer reconstruction on the full $H_2O$ acquisition is visualized in Figure 5.7. Comparing these CSI images with the images from Figure 5.3, this Roemer reconstructed result and the $SNR$-phase combined result correspond quite well. The first significant dissimilarity that can be observed is the global amplitude difference. Even though, the relative spatial profile is preserved over the multiple diffusion scans, this should not entail any problems. The second dissimilarity that can be observed is a slight difference in intensity between the voxels including more detected noise outside the VOI. We argue that this is the result of the more sensitive Roemer reconstruction than the $SNR$-phase combination method. From these CSI images the $ADC$-map is calculated by direct PM and compared with the $SNR$-phase combination benchmark from subsection 5.2.2. As can be observed in Figure 5.8, the resulting $ADC$-map calculated with the Roemer reconstruction shows close resemblance to the $SNR$-phase combined $ADC$-map. Although again, a slight overestimation with respect to the benchmark $ADC$-map can be observed.

### 5.2.4. Phase Encoding Undersampling Pattern

In order for CS-PM to be able to reconstruct the missing samples in $k$-space depicted by the generated PE undersampling pattern, this pattern must satisfy the condition that the resulting aliasing will induce only incoherent noise-like artifacts. This has been evaluated by generating multiple sets of pseudo-random PE undersampling patterns: seven sets for each PE reduction factor: $R = \{2,\ 3,\ 4\}$. These patters are enforced on the data and the difference with the full acquired data is visualized. This is evaluated before and after the DW-CSI post-processing on the whole spectra and the estimated pole magnitude, respectively. The results are displayed in histograms in Figures A.1 and A.2 of Appendix A. In these figures the distributions of the normalized aliasing induced errors in image space can be examined. These distributions are visualized for each diffusion condition, each PE reduction factor and each set of pseudo-random PE undersampling patterns. In the spectra histograms of Figure A.1, it can be observed that all sets have their mode at zero and the introduced error is centered around this mode. There are, however, a few PE undersampling patterns that evidently introduce a positive bias. The histograms of Figure A.2 show the aliasing introduced errors after post-processing on the $H_2O$ signal. These results were generated with the same PE undersampling patterns as the results from Figure A.1. From the results of Figure A.2 it can be observed that the DW-CSI post-processing introduces a bias with an increased tend to overestimation. From the histograms of Figure A.2 each first (most left) set of PE undersampling patterns is further examined in image space, the resulting aliasing induced errors are visualized in the DW-CSI images in Figures 5.9a - 5.9c for $R = 2$ to 4, respectively. Considering the already limited FOV, it is difficult to conclude whether the induced aliasing is sufficient noise-like and incoherent besides the already noted bias. However we argue that for our proof of concept, from these results we can conclude that for most generated PE undersampling patterns these patterns induce sufficiently incoherent and noise-like artifacts.

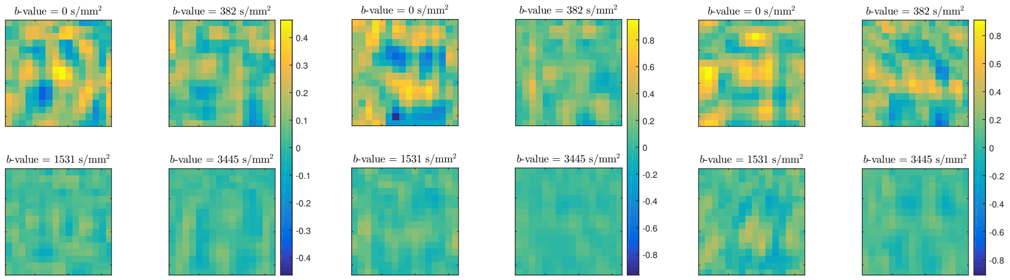

(a) $R = 2$. (b) $R = 3$. (c) $R = 4$.

Figure 5.9: PE undersampling error of $H_2O$ DW-CSI images after post-processing with $SNR$-phase combination [a.u.].

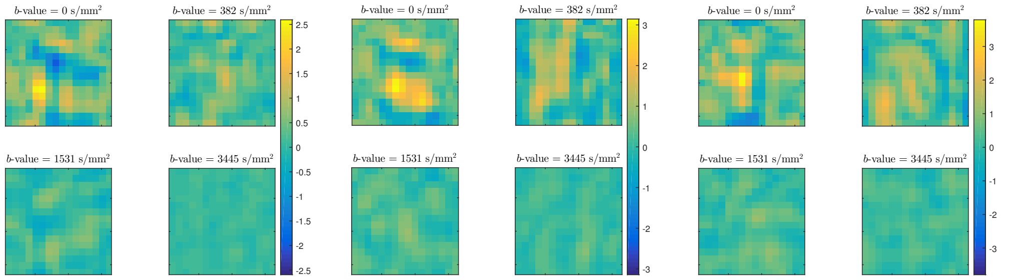

(a) $R = 2$. (b) $R = 3$. (c) $R = 4$.

Figure 5.10: PE undersampling error of $H_2O$ DW-CSI images after post-processing with Roemer reconstruction [a.u.].

An equal analysis has been performed to evaluate the effect of the Roemer reconstruction on the performance of the PE undersampling patterns. The distributions of the normalized aliasing induced errors in image space after applying the Roemer reconstruction are visualized in Figures B.1 and B.2 of Appendix B, before and after the DW-CSI post-processing on the whole spectra and the estimated pole magnitude, respectively. For an objective comparison, the same sets of PE undersampling patterns are applied as in the analysis of Appendix A. When the histograms of the Roemer reconstruction are compared with the $SNR$-phase combination, it can be observed that the aliasing artifacts are more or less preserved by the Roemer reconstruction though smaller in deviation. The DW-CSI images of Figure 5.10 present the analogue analysis of the DW-CSI images of Figure 5.9 for the Roemer reconstruction with their data drawn from the first (most left) set of PE undersampling patterns of the histograms in Figure B.2 for $R = 2$ to 4, respectively. In DW-CSI images of Figures 5.10a - 5.10c it can be observed that the aliasing artifacts appear to some degree more clustered than the aliasing artifacts after the $SNR$-phase combination.

### 5.2.5. Compressed Sensing Parameter Mapping

To evaluate the compressed sensing parameter mapping reconstruction algorithm, first the global minimum of the compressed sensing procedure is determined. This is not per se equal to the direct parameter mapped result on the full acquired $H_2O$ dataset ($R = 1.0$) for two reasons: first because with each iteration CS-PM also acts as a noise reduction algorithm in the parameter direction of each voxel; and second because CS-PM also tries to estimate the frequency components outside the circular $k$-space coverage of the full acquisition, the corners of $k$-space. The result is illustrated in Figure 5.12b where it is compared with the benchmark generated by the direct parameter mapping on the full acquired dataset from Subsection 5.2.2 as visualized in Figure 5.12a. The difference between these two $ADC$-maps is sufficiently small as can visually be observed, as also confirmed by the corresponding difference map of Figure 5.12c and the NRMSE of 0.0078.

Subsequently, the PE reduction factor $R$ is increased to 1.5, 2.0, 2.5 and 3.0. Their outcomes are illustrated in Figures 5.12d - 5.12k. From these resulting $ADC$-maps with their corresponding difference maps and NRMSEs, it is evident that an acceleration factor of $R = 1.5$ for this DW-CSI dataset is achievable with reasonable visual and numerical accuracy (NRMSE = 0.064). For higher acceleration factors it is noticeable that the CS-PM reconstruction visually does not comply with the benchmark anymore. This is emphasized by the NRMSE values which exceed 0.10 for $R > 1.5$. An argumentation for this limited acceleration is the already limited data size of DW-CSI. This limited data size makes it difficult for the PE undersample pattern to only acquire the principal data components and subsequent for CS to reconstruct the full data from these measured data components. Remarkable is difference in NRMSE of the $R = 3$ and $R = 2.5$ reconstructions, where counter intuitively the reconstruction on the further PE reduced scan performs better. This is, most likely, because in the further reduction of PEs, the PE undersampling pattern discarded profitably just the proper encodings to satisfy the CS incoherence conditions to a greater degree than with the $R = 2.5$ PE reduction.

The run time over all the computations from reading the raw data to reconstructing an $ADC$-map was approximately 110 seconds, where the CS-PM algorithm occupied approximately 15 seconds of the total run time.

The performance of the CS-PM algorithm was also evaluated on the $H_2O$ dataset after the Roemer reconstruction. As valid comparison, the estimated $ADC$-map of Subsection 5.2.3 is used as benchmark and the same PE undersampling pattern set of of the previous analysis is applied. Again the reconstruction on the non-PE reduced dataset resembles the benchmark adequately well, as can be observed in Figures 5.13a - 5.13c. However, if the acceleration factor is increased, the estimated $ADC$-maps start to diverge from the benchmark rapidly. Observing the $R = 1.5$ reconstruction, the resemblance with the benchmark is still visible apart from one significantly overestimated voxel that sequentially overshadows the other voxels. The reconstructions for $R > 1.5$ do not visually comply with the benchmark anymore. Where as assumed in Chapter 4, that the use of Roemer reconstruction with the coil sensitivity maps should increase the accuracy with respect to the $SNR$-phase combination, the performance evidently decreases when applied on an undersampled dataset.

The computation time from raw data to $ADC$-map with the Roemer reconstruction and the calculation of the CSMs increased to approximately 180 seconds, where the CS-PM algorithm remained approximately 15 seconds.

### 5.2.6. Regularization

The effect of the regularisation term $\mathbf{H}$ of Subsection 4.2.6 on $k$-$p$ space is demonstrated in Figure 5.11. This figure depicts the result of the CS-PM algorithm without the use of this regularization term on the full circular $k$-space acquired $H_2O$ data after 500 iterations. In this reconstruction, CS-PM only estimates the non-acquired peripheral $k$-spacePEs. In Figure 5.11 it becomes clear that all the voxel-wise operations of the CS-PM algorithm direct the data to a minimum-norm solution that is inconsistent with the expected medical physics. Thus, to maintain the spatial coherence of the DW-CSI images, coupling between the voxels is required in the CS-PM reconstruction.

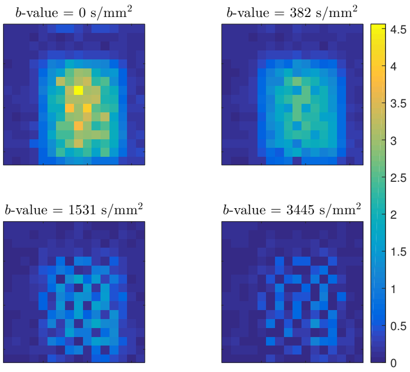

Figure 5.11: DW-CSI image of CS-PM reconstruction without regularization on $H_2O$ scan without PE reduction ($R = 1$) and 500 iterations [a.u.].

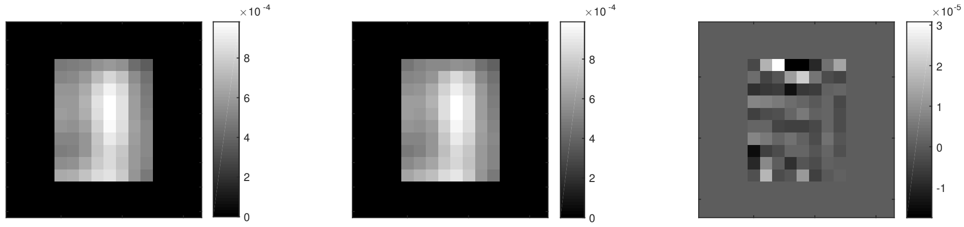

(a) Benchmark *ADC*-map by PM.

(b) Estimated *ADC*-map; $R = 1.0$; NRMSE = 0.0078.

(c) Difference; $R = 1.0$.

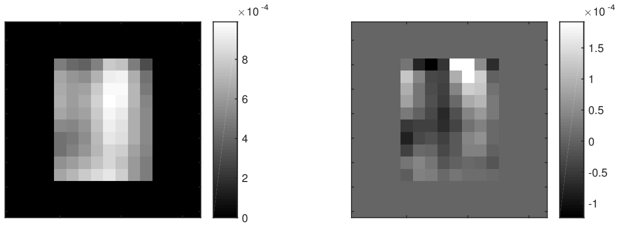

(d) Estimated *ADC*-map; $R = 1.5$; NRMSE = 0.064.

(e) Difference; $R = 1.5$.

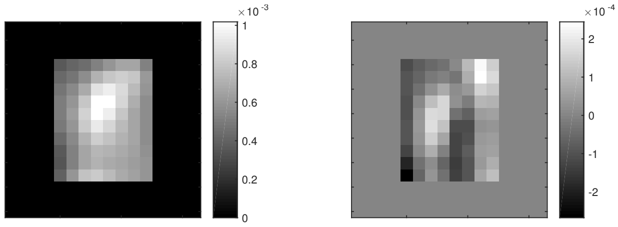

(f) Estimated *ADC*-map; $R = 2.0$; NRMSE = 0.10.

(g) Difference; $R = 2.0$.

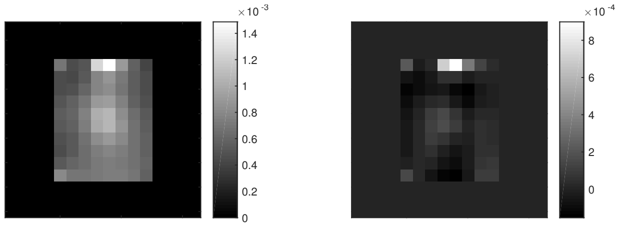

(h) Estimated *ADC*-map; $R = 2.5$; NRMSE = 0.15.

(i) Difference; $R = 2.5$.

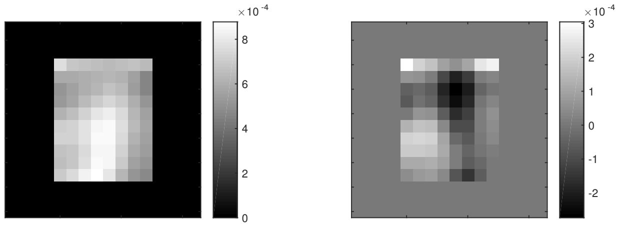

(j) Estimated *ADC*-map; $R = 3.0$; NRMSE = 0.13.

(k) Difference; $R = 3.0$.

Figure 5.12: CS-PM on $H_2O$ scan with $SNR$-phase combination, increasing acceleration factor $R$ and 500 iterations [mm$^2$/s]. **(a)** Direct PM without PE reduction; **(b)** - **(k)** CS-PM reconstructions with $R = \{1.0,\ 1.5,\ 2.0,\ 2.5,\ 3.0\}$ and their corresponding difference maps.

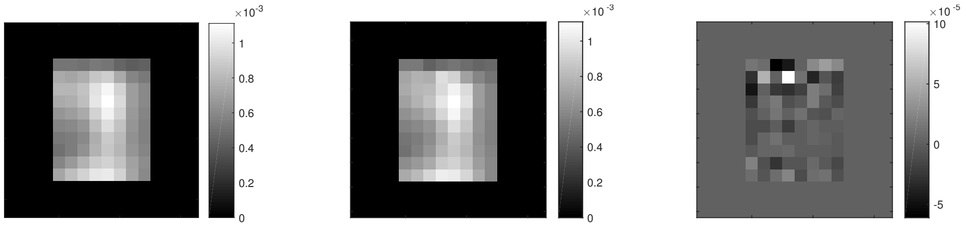

(a) Benchmark $ADC$-map by CSM-PM.

(b) Estimated $ADC$-map; $R = 1.0$; NRMSE = 0.019.

(c) Difference; $R = 1.0$.

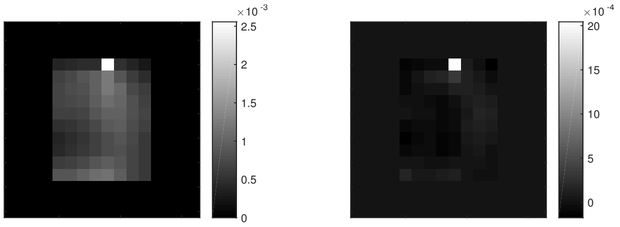

(d) Estimated $ADC$-map; $R = 1.5$; NRMSE = 0.22.

(e) Difference; $R = 1.5$.

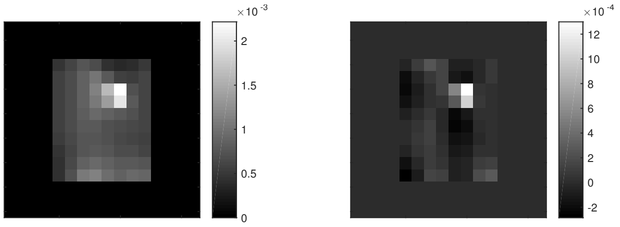

(f) Estimated $ADC$-map; $R = 2.0$; NRMSE = 0.20.

(g) Difference; $R = 2.0$.

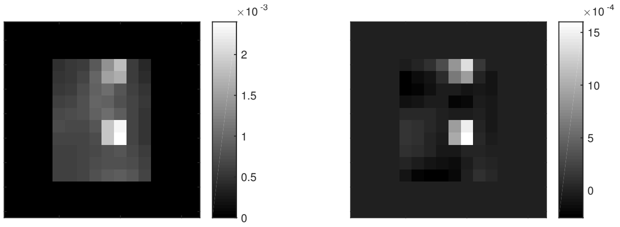

(h) Estimated$ADC$-map; $R = 2.5$; NRMSE = 0.33.

(i) Difference; $R = 2.5$.

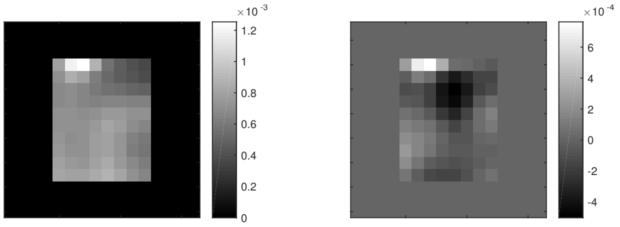

(j) Estimated $ADC$-map; $R = 3.0$; NRMSE = 0.18.

(k) Difference; $R = 3.0$.

Figure 5.13: CS-PM on $H_2O$ scan with Roemer reconstruction, increasing acceleration factor $R$ and 500 iterations [$mm^2/s$]. **(a)** Direct PM without PE reduction; **(b)** - **(k)** CS-PM reconstructions with $R = \{1.0,\ 1.5,\ 2.0,\ 2.5,\ 3.0\}$ and their corresponding difference maps.

# 6

# Discussion & Conclusion

The compressed sensing parameter mapping reconstruction algorithm has been implemented and demonstrated for the application of diffusion-weighted chemical shift imaging. From the results, an acceleration factor of $R = 1.5$ with the conventional $SNR$-phase combination presented the most clinical informative and reliable reconstruction for $R > 1$. Although this achieved acceleration factor might not sound like much, it will still save 20 minutes on a one hour scan.

A notable observation, is that the implementation of the Roemer reconstruction does not improve the accuracy after CS-PM reconstruction on a PE reduced dataset, in fact its effect on the data appears to corrupt the CS-PM reconstruction. The reason the linear Roemer reconstruction does not contribute to the performance of CS-PM is expected because the Roemer reconstruction is applied in image space. It is hypothesized that all the operations applied on the data in another domain than $k$-space before CS-PM, make up one of the three main factors of limitation on the performance of CS-PM. This is due to the fact that operations applied in another domain than $k$-space on the undersampled data, will lead to information 'leakage' to the non-PE acquired locations in $k$-space. This information is not preserved in the CS-PM reconstruction since it is not included in the data consistency term. The same holds for the DW-CSI post-processing steps that are applied in image space (steps (d), (e) and (f)). Several approaches could resolve this limitation on CS-PM. A recommended approach is to reformulate all the DW-CSI post-processing in $k$-space and to incorporate the Roemer reconstruction in the iterative CS-PM algorithm. In this fashion, the DW-CSI post-processing is applied on the acquired $k$-space of each parallel receive coil separately and the resulting $k$-$p$ space for each coil is adopted as data consistency term in the CS reconstruction. The Roemer reconstruction in the CS-PM scheme then combines and divides the separate coil data with each iteration. Another approach would be to combine the parallel measurements with the conventional $SNR$-phase combination or another algorithm applied in $k$-space and to apply the CS reconstruction in the post-processing between steps (c) and (d) on the whole spectroscopic dataset. Parameter mapping can eventually estimate the $ADC$-values.

A second limitation on CS-PM is the already limited data size in the full acquisition. Since the $k$-space matrix is spatially only $12 \times 12$, it becomes complicated to discard a significant portion of the phase encodings and to still acquire the principal signal components to reconstruct the whole dataset. This could on the other hand imply that it is possible to increase the effective FOV and VOI without increasing the scan time.

The third limitation on the performance of CS-PM is imposed by the applied PE undersampling patterns. Further research can determine if and which generated undersampling patterns are suitable to measure the DW-CSI principal data components and to imply sufficient incoherence in the resulting aliasing for an effective PE reduction and proper reconstruction. An evaluation of the point spread function of the undersampling patterns could function as measure of imposed incoherence [6]. The use of the undersampling patterns can be further enhanced when combined with the navigator accept/reject strategy. In this way, dynamic undersampling patterns are imposed on the acquisition, while the design and performance of the undersampling pattern are monitored and adjusted according to the point spread function in real time.

With these discussed limitations further studied and resolved, the algorithm should be evaluated on more datasets to prevent overfitting on the limited training data and to further tailor it for the diffusion of the metabolites of interest. Furthermore, to test the stability of CS-PM, a noise-imposing Monte-Carlo simulation on the algorithm could provide this valuable insight.

Further improvement can be achieved by considering and investigating other regularisation methods that work efficiently on these small datasets. Another asset that could boost the performance of CS-PM is to complement non-acquired PEs as complex conjugates from their mirror $k$-space data as initial guess for CS.

In conclusion, the acceleration of DW-CSI still requires a lot of work, however, let this thesis be a first step in right direction.

# Bibliography

[1] A. E. Ercan, A. Techawiboonwong, M. J. Versluis, A. G. Webb, and I. Ronen, "Diffusion-weighted chemical shift imaging of human brain metabolites at 7T." *Magnetic Resonance in Medicine*, vol. 73, no. 6, pp. 2053–2061, 2015. [Online]. Available: http://www.ncbi.nlm.nih.gov/pubmed/24986121

[2] S. Posse, C. A. Cuenod, and D. Le Bihan, "Human brain: proton diffusion MR spectroscopy." *Radiology*, vol. 188, no. 3, pp. 719–25, 1993. [Online]. Available: http://www.ncbihttp//www.ncbi.nlm.nih.gov/pubmed/8351339

[3] I. Ronen and J. Valette, "Diffusion-Weighted Magnetic Resonance Spectroscopy," pp. 733–750, 2015. [Online]. Available: http://doi.wiley.com/10.1002/9780470034590.emrstm1471

[4] C. Najac, F. Branzoli, I. Ronen, and J. Valette, "Brain intracellular metabolites are freely diffusing along cell fibers in grey and white matter, as measured by diffusion-weighted MR spectroscopy in the human brain at 7 T," *Brain Structure and Function*, vol. 221, no. 3, pp. 1245–1254, apr 2016. [Online]. Available: http://link.springer.com/article/10.1007/s00429-014-0968-5

[5] R. M. Heidemann, Ö. Özsarlak, P. M. Parizel, J. Michiels, B. Kiefer, V. Jellus, M. Müller, F. Breuer, M. Blaimer, M. A. Griswold, P. M. Jakob, O. Ozsarlak, P. M. Parizel, J. Michiels, B. Kiefer, V. Jellus, M. Muller, F. Breuer, M. Blaimer, M. A. Griswold, and P. M. Jakob, "A brief review of parallel magnetic resonance imaging," *European Radiology*, vol. 13, no. 10, pp. 2323–2337, 2003.

[6] M. Lustig, D. L. Donoho, and J. M. Pauly, "Sparse MRI: The application of compressed sensing for rapid MR imaging," *Magnetic Resonance in Medicine*, vol. 58, no. 6, pp. 1182–1195, 2007.

[7] A. Ghosh, "Magnetic Resonance Imaging or MRI," 2012. [Online]. Available: https://thecustomizewindows.com/2012/04/magnetic-resonance-imaging-or-mri/

[8] J. L. Prince and J. Links, *Medical Imaging Signals and Systems*, ser. Pearson Prentice Hall bioengineering. Pearson Prentice Hall, 2006. [Online]. Available: https://books.google.nl/books?id=IPm8QgAACAAJ

[9] C. L. Epstein, *Introduction to the Mathematics of Medical Imaging*, 2nd ed. Society for Industrial and Applied Mathematics, 2008.

[10] A. Skoch, F. Jiru, and J. Bunke, "Spectroscopic imaging: Basic principles," *European Journal of Radiology*, vol. 67, no. 2, pp. 230–239, 2008.

[11] I. Tkáč, Z. Starčuk, I. Y. Choi, and R. Gruetter, "In vivo 1H NMR spectroscopy of rat brain at 1 ms echo time," *Magnetic Resonance in Medicine*, vol. 41, no. 4, pp. 649–656, 1999.

[12] P. A. Bottomley, "Spatial localization in NMR spectroscopy in vivo." *Annals of the New York Academy of Sciences*, vol. 508, pp. 333–348, 1987.

[13] D. Hoa, "Single voxel spectroscopy (SVS)," 2016. [Online]. Available: https://www.imaios.com/en/e-Courses/e-MRI/Magnetic-Resonance-Spectroscopy-MRS/single-voxel-spectroscopy

[14] E. O. Stejskal and J. E. Tanner, "Spin diffusion measurements: spin echoes in the presence of a time-dependant field gradient," *The Journal of chemical physics*, vol. 42, no. 1, p. 5, 1965.

[15] M. E. Wagshul, P. K. Eide, and J. R. Madsen, "The pulsating brain: A review of experimental and clinical studies of intracranial pulsatility." *Fluids and barriers of the CNS*, vol. 8, no. 1, p. 5, 2011. [Online]. Available: http://www.ncbi.nlm.nih.gov/pmc/articles/PMC3042979/

[16] L. Vanhamme, R. D. Fierro, S. Van Huffel, and R. de Beer, "Fast Removal of Residual Water in Proton Spectra," *Journal of magnetic resonance (San Diego, Calif. : 1997)*, vol. 132, no. 2, pp. 197–203, 1998. [Online]. Available: http://www.ncbi.nlm.nih.gov/pubmed/9632545

[17] S. W. Provencher, "Estimation of metabolite concentrations from localized in vivo proton NMR spectra," *Magnetic Resonance in Medicine*, vol. 30, no. 6, pp. 672–679, 1993. [Online]. Available: http://doi.wiley.com/10.1002/mrm.1910300604

[18] D. J. Larkman and R. G. Nunes, "Parallel magnetic resonance imaging." *Physics in Medicine and Biology*, vol. 52, no. 7, pp. R15–R55, 2007.

[19] A. Deshmane, V. Gulani, M. A. Griswold, and N. Seiberlich, "Parallel MR imaging," *Journal of Magnetic Resonance Imaging*, vol. 36, no. 1, pp. 55–72, 2012.

[20] M. A. Griswold, P. M. Jakob, R. M. Heidemann, M. Nittka, V. Jellus, J. Wang, B. Kiefer, and A. Haase, "Generalized Autocalibrating Partially Parallel Acquisitions (GRAPPA)," *Magnetic Resonance in Medicine*, vol. 47, no. 6, pp. 1202–1210, 2002.

[21] K. P. Pruessmann, M. Weiger, M. B. Scheidegger, and P. Boesiger, "SENSE: Sensitivity encoding for fast MRI," *Magnetic Resonance in Medicine*, vol. 42, no. 5, pp. 952–962, 1999.

[22] U. Dydak, M. Weiger, K. P. Pruessmann, D. Meier, and P. Boesiger, "Sensitivity-Encoded Spectroscopic Imaging," *Magnetic Resonance in Medicine*, vol. 722, no. 46, pp. 713–722, 2001.

[23] S. Posse, R. Otazo, S.-Y. Tsai, A. E. Yoshimoto, and F.-H. Lin, "Single-shot magnetic resonance spectroscopic imaging with partial parallel imaging." *Magnetic Resonance in Medicine*, vol. 61, no. 3, pp. 541–547, 2009.

[24] R. Birch, A. C. Peet, T. N. Arvanitis, and M. Wilson, "Sensitivity encoding for fast 1H MR spectroscopic imaging water reference acquisition," *Magnetic Resonance in Medicine*, vol. 00, pp. n/a–n/a, 2014. [Online]. Available: http://doi.wiley.com/10.1002/mrm.25355

[25] D. L. Donoho, "Compressed sensing," *IEEE Transactions on Information Theory*, vol. 52, no. 4, pp. 1289–1306, 2006. [Online]. Available: http://ieeexplore.ieee.org/xpl/articleDetails.jsp?arnumber=1614066

[26] Y. Tsaig and D. L. Donoho, "Extensions of compressed sensing," *Signal Processing*, vol. 86, no. 3, pp. 549–571, 2006. [Online]. Available: http://www.sciencedirect.com/science/article/pii/S0165168405002215

[27] M. Lustig, D. L. Donoho, J. M. Santos, and J. M. Pauly, "Compressed sensing MRI: A look at how CS can improve on current imaging techniques," *IEEE Signal Processing Magazine*, vol. 25, no. 2, pp. 72–82, 2008.

[28] I. Daubechies, "The wavelet transform, time-frequency localization and signal analysis," *Transactions on Information Theory, IEEE*, vol. 36, no. 5, pp. 961–1005, 1990.

[29] P. Cao and E. X. Wu, "Accelerating phase-encoded proton MR spectroscopic imaging by compressed sensing." *Journal of Magnetic Resonance Imaging*, vol. 00, pp. 1–9, 2014. [Online]. Available: http://www.ncbi.nlm.nih.gov/pubmed/24436225

[30] M. Lustig, "Sparse MRI," Ph.D. dissertation, Stanford University, 2008.

[31] S. S. Vasanawala, M. J. Murphy, M. T. Alley, P. Lai, K. Keutzer, J. M. Pauly, and M. Lustig, "Practical parallel imaging compressed sensing MRI: Summary of two years of experience in accelerating body MRI of pediatric patients," *Proceedings - International Symposium on Biomedical Imaging*, pp. 1039–1043, 2011.

[32] M. Lustig and J. M. Pauly, "SPIRiT: Iterative self-consistent parallel imaging reconstruction from arbitrary k-space." *Magnetic Resonance in Medicine*, vol. 64, no. 2, pp. 457–71, 2010. [Online]. Available: http://doi.wiley.com/10.1002/mrm.22428

[33] M. Uecker, P. Lai, M. J. Murphy, P. Virtue, M. Elad, J. M. Pauly, S. S. Vasanawala, and M. Lustig, "ESPIRiT - An eigenvalue approach to autocalibrating parallel MRI: Where SENSE meets GRAPPA," *Magnetic Resonance in Medicine*, vol. 71, no. 3, pp. 990–1001, 2014. [Online]. Available: http://doi.wiley.com/10.1002/mrm.24751

[34] M. Uecker, T. Zhang, F. Ong, M. Lustig, J. I. Tamir, D. Bahri, P. Virtue, and J. Y. Cheng, "BART: version 0.2.09," oct 2015. [Online]. Available: http://zenodo.org/record/31907

[35] J. I. Tamir, F. Ong, J. Y. Cheng, M. Uecker, and M. Lustig, "Generalized Magnetic Resonance Image Reconstruction using The Berkeley Advanced Reconstruction Toolbox," in *Proceedings of the ISMRM 2016 Data Sampling and Image Reconstruction Workshop*, vol. 2486. Sedona, AZ, USA: ISMRM (International Society for Magnetic Resonance in Medicine), 2016, p. 9660006. [Online]. Available: http://www.ismrm.org/workshops/Data16/

[36] M. Doneva, P. Börnert, H. Eggers, C. Stehning, J. Sénégas, and A. Mertins, "Compressed sensing reconstruction for magnetic resonance parameter mapping," *Magnetic Resonance in Medicine*, vol. 64, no. 4, pp. 1114–1120, 2010.

[37] M. Doneva, “Advances in Compressed Sensing for Magnetic Resonance Imaging,” Ph.D. dissertation, University of Lübeck, 2011.

[38] W. Li, M. A. Griswold, and X. Yu, “Fast cardiac T1 mapping in mice using a model-based compressed sensing method.” *Magnetic Resonance in Medicine*, vol. 68, no. 4, pp. 1127–34, 2012. [Online]. Available: http://www.ncbi.nlm.nih.gov/pmc/articles/PMC3324650/

[39] B. Bilgic, K. Setsompop, J. Cohen-Adad, A. Yendiki, L. L. Wald, and E. Adalsteinsson, “Accelerated diffusion spectrum imaging with compressed sensing using adaptive dictionaries,” *Magnetic Resonance in Medicine*, vol. 68, no. 6, pp. 1747–1754, 2012.

[40] D. MacKenzie, “Compressed Sensing Makes Every Pixel Count,” *Signal Processing*, vol. 7, no. July, pp. 114–127, 2007. [Online]. Available: http://www.ams.org/samplings/math-history/hap7-pixel.pdf

[41] M. I. Menzel, E. T. Tan, K. Khare, J. I. Sperl, K. F. King, X. Tao, C. J. Hardy, and L. Marinelli, “Accelerated diffusion spectrum imaging in the human brain using compressed sensing,” *Magnetic Resonance in Medicine*, vol. 66, no. 5, pp. 1226–1233, 2011.

[42] G. J. Marseille, R. de Beer, M. Fuderer, A. F. Mehlkopf, and D. van Ormondt, “Nonuniform Phase-Encode Distributions for MRI Scan Time Reduction,” *Journal of Magnetic Resonance*, vol. 111, no. 61, pp. 70–75, 1996. [Online]. Available: http://www.ncbi.nlm.nih.gov/pubmed/8661264

[43] P. B. Roemer, W. A. Edelstein, C. E. Hayes, S. P. Souza, and O. Mueller, “The NMR Phased Array,” *Magnetic Resonance in Medicine*, vol. 16, no. 2, pp. 192–225, 1990. [Online]. Available: http://dx.doi.org/10.1002/mrm.1910160203

[44] S. M. Kay, *Fundamentals of Statistical Signal Processing: Estimation Theory*, 1st ed. New Jersey: Prentice-Hall, 1993.

[45] A. Graps, “An Introduction to Wavelets,” *IEEE Computational Science and Engineering*, vol. 2, no. 2, pp. 50–61, 1995.

[46] J. Helenius, L. Soinne, J. Perkiö, O. Salonen, A. Kangasmäki, M. Kaste, R. A. Carano, H. J. Aronen, and T. Tatlisumak, “Diffusion-Weighted MR Imaging in Normal Human Brains in Various Age Groups.” *AJNR American journal of neuroradiology*, vol. 23, no. 2, pp. 194–199, 2002. [Online]. Available: http://www.ncbi.nlm.nih.gov/pubmed/11847041

[47] Y. C. Pati, R. Rezaiifar, and P. S. Krishnaprasad, “Orthogonal Matching Pursuit: Recursive Function Approximation with Applications to Wavelet Decomposition,” *IEEE*, vol. 1, pp. 40–44, nov 1993.

[48] M. Elad, *Sparse and Redundant Representations*. Springer New York, 2010, vol. 1.

# A

# Aliasing Artifact Distributions after *SNR*-Phase Combination

This appendix displays the results discussed in Subsection 5.2.4.

The histograms of Figure A.1 show the normalized aliasing induced errors of all the voxels in image space of $S^{\{\mathrm{a}\}}_{xy,m}(f)$ of Subsection 2.2.2 after the $SNR$-phase coil combination, calculated by:

$$e_{S^{\{\mathrm{a}\}}}(R) = \frac{S^{\{\mathrm{a}\}}_{xy,m}(f)\big|_{R>1} - S^{\{\mathrm{a}\}}_{xy,m}(f)\big|_{R=1}}{\left\| S^{\{\mathrm{a}\}}_{xy,m}(f)\big|_{R=1} \right\|_2} \tag{A.1}$$

The histograms of Figure A.2 show the normalized aliasing induced errors of all the voxels in image space of $\mathbf{S}$ of Subsection 4.2.2 after the $SNR$-phase coil combination, calculated by:

$$e_{\mathbf{S}}(R) = \frac{\mathbf{S}\big|_{R>1} - \mathbf{S}\big|_{R=1}}{\left\| \mathbf{S}\big|_{R=1} \right\|_2} \tag{A.2}$$

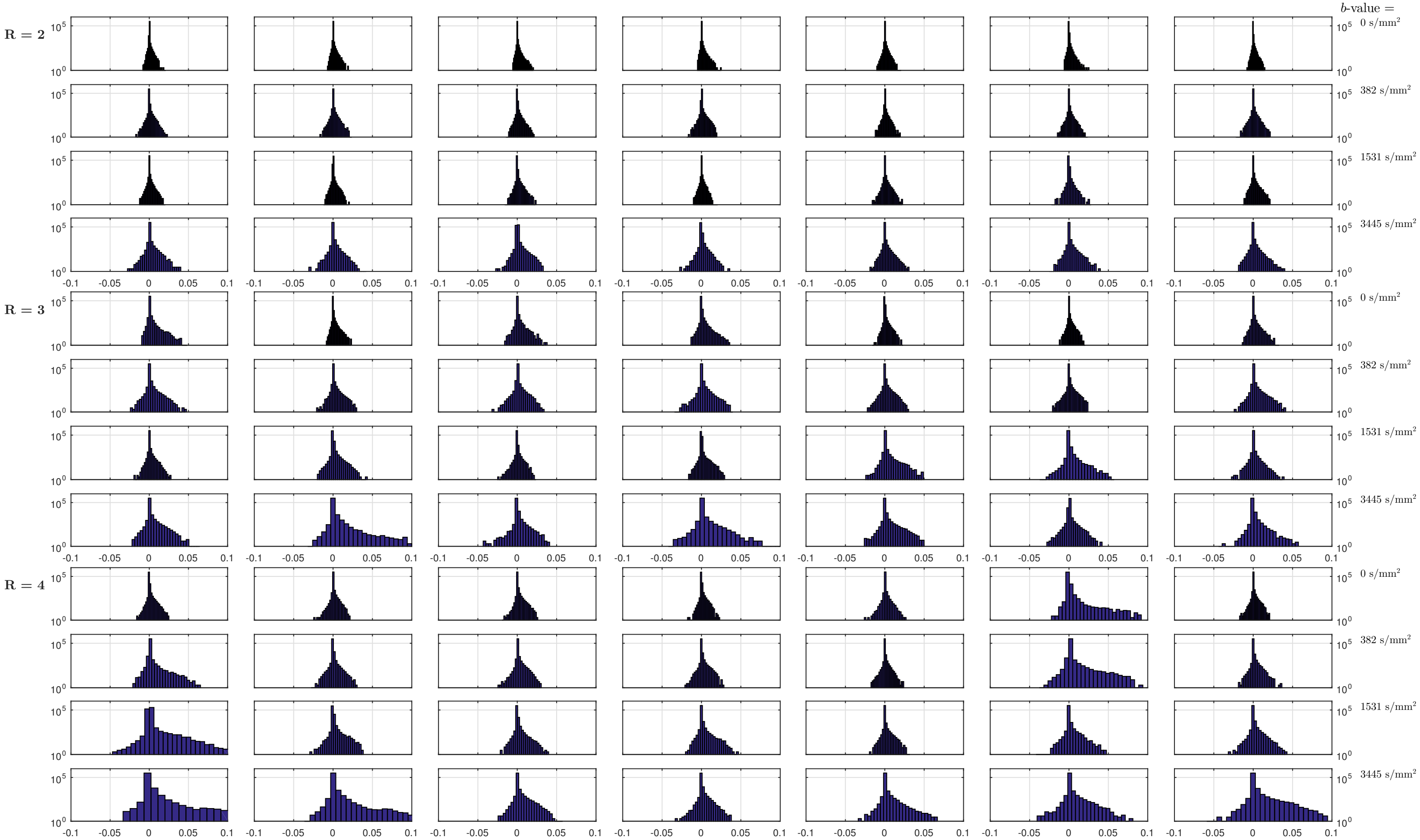

Figure A.1: Set of histograms visualizing the normalized difference in data between the PE undersampled vs full acquired **before** post-processing of spectra in image-space: equation (A.1). Each row depicts a different diffusion condition, each set of four rows a different acceleration factor ($R$), each column a different set of pseudo-random PE undersampling patterns for that $R$. Note: logarithmic scale on Y-axis.

Figure A.2: Set of histograms visualizing the normalized difference in data between the PE undersampled vs full acquired **after** post-processing in parameter-image space: equation (A.2). Each row depicts a different diffusion condition, each set of four rows a different acceleration factor (*R*), each column a different set of pseudo-random PE undersampling patterns for that *R*.

# B

# Aliasing Artifact Distributions after Roemer Reconstruction

This appendix displays the results discussed in Subsection 5.2.3.

The histograms of Figure B.1 show the normalized aliasing induced errors of all the voxels in image space of $S^{\{\mathrm{a}\}}_{xy,m}(f)$ of Subsection 2.2.2 after the Roemer reconstruction, calculated by:

$$e_{S^{\{\mathrm{a}\}}_{\mathrm{csm}}}(R) = \frac{S^{\{\mathrm{a}\}}_{xy,m}(f)\big|_{R>1} - S^{\{\mathrm{a}\}}_{xy,m}(f)\big|_{R=1}}{\left\| S^{\{\mathrm{a}\}}_{xy,m}(f)\big|_{R=1} \right\|_2} \tag{B.1}$$

The histograms of Figure B.2 show the normalized aliasing induced errors of all the voxels in image space of **S** of Subsection 4.2.2 after the Roemer reconstruction, calculated by:

$$e_{\mathbf{S}_{\mathrm{csm}}}(R) = \frac{\mathbf{S}\big|_{R>1} - \mathbf{S}\big|_{R=1}}{\left\| \mathbf{S}\big|_{R=1} \right\|_2} \tag{B.2}$$

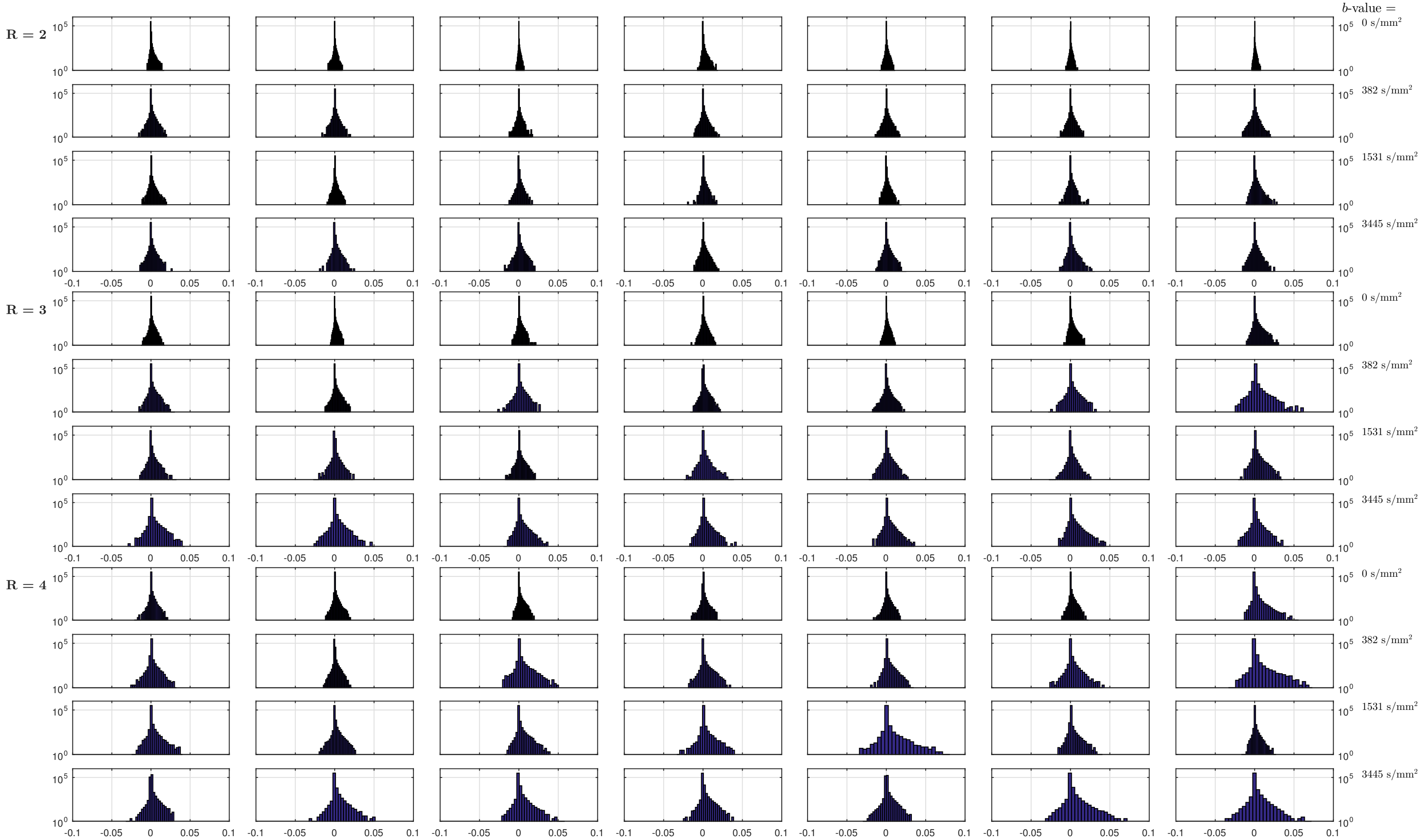

Figure B.1: Set of histograms visualizing the normalized difference in data between the PE undersampled vs full acquired **before** post-processing **after** the Roemer reconstruction of spectra in image-space: equation (B.1). Each row depicts a different diffusion condition, each set of four rows a different acceleration factor ($R$), each column a different set of pseudo-random PE undersampling patterns for that $R$. Note: logarithmic scale on Y-axis.

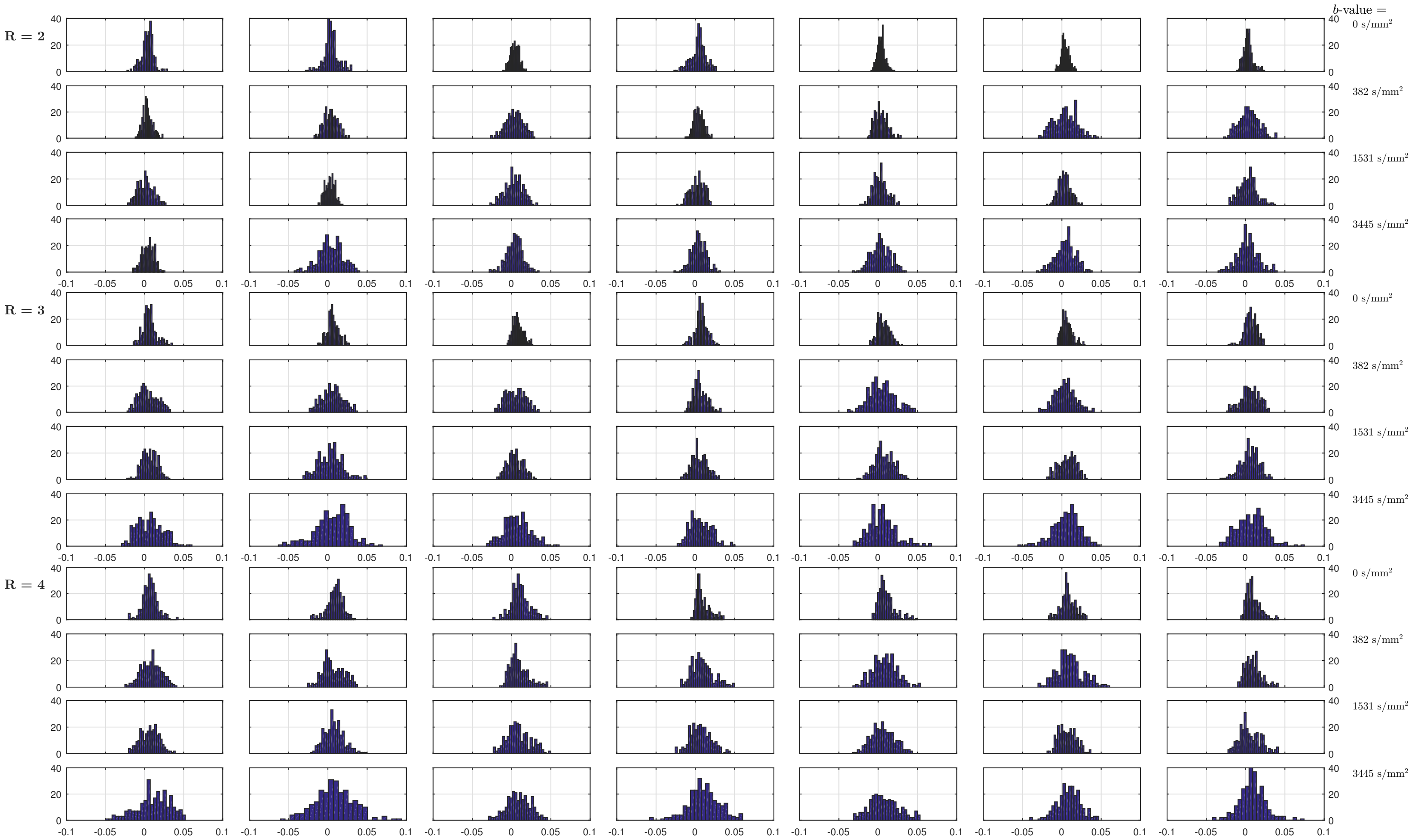

Figure B.2: Set of histograms visualizing the normalized difference in data between the PE undersampled vs full acquired **after** post-processing with the Roemer reconstruction in parameter-image space: equation (B.2). Each row depicts a different diffusion condition, each set of four rows a different acceleration factor (*R*), each column a different set of pseudo-random PE undersampling patterns for that *R*.